

Sliding-Mode Design with Disturbance Observer Optimized by Improved HBA Algorithm for Frequency Regulation of Multi-Area Power System

Gonggui Chen, Zhijin Jiang, Hao Tan, Chaohua Zhang, Jinzhu Wei, Wenchen Chen, Hongyu Long*

Abstract—The intermittency of renewable energy generation and the randomness of power load variations lead to voltage and frequency fluctuations among the interconnected power system. In this study, a control strategy based on sliding mode control theory and disturbance observer is proposed for the multi-area power system with parameter uncertainties to handle load frequency control. By choosing an appropriate integral-type sliding-mode surface and reaching law, a sliding-mode load frequency controller is constructed. In order to reduce the influence of uncertainties, a disturbance observer is designed to estimate lumped disturbances. On this basis, the sliding mode controller is reconstructed to provide better control effect. And the improved honey badger algorithm is used to tune out the optimal parameters of the designed controller. Simulation studies are carried out on a two-region reference system and an unequal capacity three-area power system with nonlinearity connected wind turbine generators to illustrate the favorable performance of the power system under the proposed control strategy. The comparison results show that the proposed control method possesses excellent frequency control ability under the uncertainty of load disturbance, wind power fluctuations and parameter uncertainties. And it also achieves efficient frequency control under a certain range of communication delay.

Index Terms—Load frequency control (LFC), sliding mode control (SMC), wind turbine generators (WTGs), honey badger algorithm (HBA), disturbance observer (DO), uncertainties

Manuscript received June 14, 2022; revised October 14, 2022. This work was supported by the National Natural Science Foundation of China under Grant 51207064.

Gonggui Chen is a professor of Key Laboratory of Industrial Internet of Things and Networked Control, Ministry of Education, Chongqing University of Posts and Telecommunications, Chongqing 400065, China; (e-mail: chenggpw@126.com).

Zhijin Jiang is a graduate student of Chongqing University of Posts and Telecommunications, Chongqing 400065, China (e-mail: jzjoo_cqupt@126.com).

Hao Tan is a senior engineer of Economic and Technology Research Institute, State Grid Chongqing Electric Power Company, Chongqing 401120, China (e-mail: tanhao_cq@163.com).

Chaohua Zhang is a senior engineer of Economic and Technology Research Institute, State Grid Chongqing Electric Power Company, Chongqing 401120, China (e-mail: zhangchaohua_cq@163.com).

Jinzhu Wei is an engineer of State Grid Chongqing Qianjiang Power Supply Company, Chongqing 409000, China (e-mail: weijinzhu_qj@163.com).

Wenchen Chen is an assistant engineer of State Grid Chongqing Qianjiang Power Supply Company, Chongqing 409000, China (e-mail: chenwenchen_qj@163.com).

Hongyu Long* is a professor level senior engineer of Chongqing Key Laboratory of Complex Systems and Bionic Control, Chongqing University of Posts and Telecommunications, Chongqing 400065, China (corresponding author to provide phone: +8613996108500; e-mail: longhongyu20@163.com).

I. INTRODUCTION

With the scarcity of fossil fuels and the growing problem of global warming, renewable energy is making up an increasing proportion of the power system [1]. As a major renewable energy source, wind energy is increasingly popularized in the interconnected power system. However, wind power generation is largely dependent on weather conditions, which may cause grand frequency deviations. Due to the increasingly complex interconnected power systems continuously connected to various energy sources, the transient stability of the system is easily affected by various electrical components, unknown modeling errors and parameter uncertainties. In addition, power systems usually consist of multiple regions, each of which can be connected to the rest by tie lines. Therefore, when there are parameter uncertainties and random load changes in the interconnected power system, severe frequency oscillations are more likely to occur in the system. In order to ensure the safe and stable operation of the interconnected power system, it is necessary to maintain power quality and balance active power flow through load frequency control [2].

At present, different control methods have been used to overcome the load frequency regulation problem, such as traditional proportional integral derivative control, internal model control, fuzzy logic control, neural networks control, model predictive control and so on [3-7]. Sliding mode control, as a powerful nonlinear robust control technology, has been widely used in various engineering practices and researches because of its characteristics of fast response, robust performance and strict control laws. Quite a few scholars have also introduced it into the control of complex power systems to maintain stability and high robustness of the power system. G. Tang et al. [8] proposed an active power modulation method based on sliding mode robust control for multi-terminal HVDC systems. K. Vrdoljak et al. [9] proposed a discrete-time sliding mode control strategy for load frequency control of hydrothermal power plants, and the simulation experiments proved that the proposed strategy had more advantages than the traditional PI control method. Considering the nonlinear nature of the power system and the uncertainty of the system, the sliding mode is often used together with the proportional-integral mechanism to make the power system stable in a large range around the normal state. Y. Mi et al. [10] designed a decentralized sliding film frequency controller for multi-region interconnected power systems with matching and mismatching determinism by constructing PI sliding mode

surfaces for each region. Of this, the integral part of the sliding mode surface forced the system state to drive to the desired equilibrium. D. Qian et al. [11] proposed an integral synovial control method for wind power generation systems, and used RBF neural network to achieve active compensation for the controller. Z. Deng and C. Xu [12] developed a terminal sliding mode controller based on derivatives and integrals for the subsystems of the multi-region interconnected power system with wind farm.

The complex structure of the power system exacerbates the uncertainty of the LFC problem. It is necessary to construct a disturbance observer to improve the control precision of the controller and achieve better control performance. The main idea of the observer is to estimate the unknown term, which concentrates the internal and external uncertainties of the model. This property of the observer provides an excellent idea for dealing with internal and external disturbances and uncertainties in power systems. It avoids the previous disadvantages of designing controllers with unknown or imprecise boundary values.

Meanwhile, combining with a reasonable control optimization design, the proposed controller can have more advantages in coping with various anomalies and uncertainties. To this end, a series of intelligent optimization algorithms is a good approach to solve the above issues [13-15]. E. S. Ali et al. [16] optimized load frequency controllers for interconnected power systems by using bacterial foraging algorithms. M. Shouran et al. [17] proposed a sliding mode variable structure design method for load frequency control of two-region power systems. To achieve the optimal use of the proposed controller, a honeybee optimization algorithm is employed to adjust the controller parameters. B. Mohanty [18] designed an output feedback sliding mode controller for a multi-region and multi-source interconnected power system, and used teaching and learning based optimization (TLBO) technology to optimize the feedback gain and switching vector of the controller. K.Premkumar et al. [19] introduced a fuzzy proportional derivative controller in the brushless DC speed control system, and used a variety of metaheuristic algorithms to optimize the controller. Then the simulation results shown that the fuzzy proportional derivative (FPD) control strategy optimized by bats had the best performance in this engineering practice. Easy to spot, it is difficult for a specific algorithm to have good performance in every particular problem. Nevertheless, newly developed optimization techniques frequently have better performance while possessing the advantages and characteristics of mature technologies.

On the basis of the above research, this study proposes a SMC control strategy optimized by the improved honey badger algorithm (IHBA), which is based on the disturbance observer, trying to apply sliding mode control to the automatic generation control (AGC) problem.

The main contributions of this study are as follows :

(i) In this study, the perturbations and parameter uncertainties are modeled in the LFC model and an integral sliding mode is designed to tune the frequency of the system with good control capability for multi-area interconnected power systems. It can improve the stability and robustness of the system.

(ii) A disturbance observer is constructed in an attempt to improve the tracking accuracy, estimate the external disturbance and system uncertainty, and expand the control bandwidth, which is a major shortcoming of the basic sliding mode. Based on the estimated disturbance value, a new sliding mode surface is designed to reconstruct the sliding mode controller. Then, a discontinuous control law with high-frequency switching gain is designed so that the initial state can reach the sliding mode surface.

(iii) By introducing inertial weights, mirror population selection and levy flight, improved HBA is proposed to tune the parameters of the designed integral sliding mode controller.

(iv) To verify the effectiveness of the proposed strategy, it is extended to the unequal power three-region power system, where nonlinear GRC link is considered and WTGs are connected into the system.

The rest of this paper is organized as follows. Section II states models of power systems with parametric uncertainties. Section III presents the detailed design process of the disturbance observer-based SMC scheme and the IHBA-based control scheme. Section IV, simulations are carried out in a multi-region power system to verify the effectiveness of the proposed strategy. Section V concludes this article.

II. MULTI-AREA POWER SYSTEM MODEL

A. LFC Model

Figure 1 is a block diagram of the control model of the i -th area of the multi-area interconnected power system. The actual power system is a complex nonlinear dynamic system. However, only slow and subtle changes will appear in loads and resources during the normal operation of power system. As a result, linearization of the model is allowed in load frequency control.

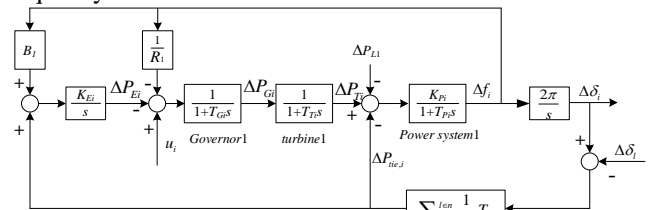


Fig. 1. Transfer function model of the i -th area in multi-area power system

In this study, a LFC model is designed, which is similar to the literature [10, 20]. For a multi-region interconnected power system, the frequency controller adjusts the governor through the tie-line power deviation and regional frequency deviation, and then reduces the area control error (ACE) by adjusting the turbine opening. The frequency deviations of all interconnected regions are coordinated by setting it to zero. For region- i , define the area control error as

$$ACE_i(t) = \Delta P_{tie,i}(t) + B_i \Delta f_i(t) \quad (1)$$

The frequency dynamics equation for area- i is described as

$$\dot{\Delta f}_i(t) = \frac{K_{Pi}}{T_{Pi}} \left[\Delta P_{Ti}(t) - \Delta P_{Di}(t) - \frac{1}{2\pi} \Delta P_{tie,i}(t) - \frac{K_{Pi}}{T_{Pi}} \Delta f_i(t) \right] \quad (2)$$

Where

$$\Delta \dot{P}_{Ti}(t) = \frac{1}{T_{Ti}} \Delta P_{Gi}(t) - \frac{1}{T_{Ti}} \Delta P_{Ti}(t) \quad (3)$$

$$\Delta \dot{P}_{Gi}(t) = \frac{1}{T_{Gi}} \left[u_i(t) - \Delta P_{Ei}(t) - \Delta P_{Gi}(t) - \frac{1}{R_i} \Delta f_i(t) \right] \quad (4)$$

$$\Delta \dot{P}_{Ei}(t) = K_{Ei} \left\{ B_i \Delta f_i(t) + \frac{1}{2\pi} \sum_{\substack{l \in N \\ l \neq i}} T_{il} [\Delta \delta_l(t) - \Delta \delta_i(t)] \right\} \quad (5)$$

$$\Delta \dot{\delta}_i(t) = 2\pi \Delta f_i(t) \quad (6)$$

According to the power system model of each region, the state variables of the power system under study are obtained, which are denoted as $x_i(t) = [\Delta f_i(t), \Delta P_{Ti}(t), \Delta P_{Gi}(t), \Delta P_{Ei}(t), \Delta \delta_i(t)]^T \in R^m$. They respectively represent the frequency deviation, generator output, governor valve position, integral control and rotor angle deviation, m represents the state number of the studied power system, and the state equation of the system model is as follows

$$\begin{aligned} \dot{x}_i(t) &= A_i x_i(t) + B_i u_i(t) + \sum_{\substack{l \in N \\ l \neq i}} C_{il} x_l(t) + D_i \Delta P_{Di}(t) \\ &= \begin{bmatrix} -\frac{1}{T_{Pi}} & \frac{K_{Pi}}{T_{Pi}} & 0 & 0 & -\frac{K_{Pi}}{2\pi T_{Pi}} \sum_{\substack{l \in N \\ l \neq i}} T_{il} \\ 0 & -\frac{1}{T_{Ti}} & \frac{1}{T_{Ti}} & 0 & 0 \\ -\frac{1}{R_i T_{Gi}} & 0 & -\frac{1}{T_{Gi}} & -\frac{1}{T_{Gi}} & 0 \\ K_{Ei} B_i & 0 & 0 & 0 & \frac{K_{Ei}}{2\pi} \sum_{\substack{l \in N \\ l \neq i}} T_{il} \\ 2\pi & 0 & 0 & 0 & 0 \end{bmatrix} \begin{bmatrix} \Delta f_i \\ \Delta P_{Ti} \\ \Delta P_{Gi} \\ \Delta P_{Ei} \\ \Delta \delta_i \end{bmatrix} \\ &+ \begin{bmatrix} 0 \\ 0 \\ \frac{1}{T_{Gi}} \\ 0 \\ 0 \end{bmatrix} u_i + \begin{bmatrix} 0 & 0 & 0 & 0 & \frac{K_{Pi}}{2\pi T_{Pi}} T_{il} \\ 0 & 0 & 0 & 0 & 0 \\ 0 & 0 & 0 & 0 & 0 \\ 0 & 0 & 0 & 0 & -\frac{K_{Ei}}{2\pi T_{Pi}} T_{il} \\ 0 & 0 & 0 & 0 & 0 \end{bmatrix} \begin{bmatrix} \Delta f_l \\ \Delta P_{Ti} \\ \Delta P_{Gi} \\ \Delta P_{Ei} \\ \Delta \delta_l \end{bmatrix} + \begin{bmatrix} -\frac{K_{Pi}}{T_{Pi}} \\ 0 \\ 0 \\ 0 \\ 0 \end{bmatrix} \Delta P_{Di} \quad (7) \end{aligned}$$

In (7), $x_i(t) \in R^m$ is the state vector, $u_i(t) \in R^n$ is the state vector of the adjacent area, $u_i(t) \in R^n$ is the control output vector, $\Delta P_{Di}(t) \in R^k$ is the load disturbance vector. T_{Ti} , T_{Gi} , T_{Pi} are the time constants of the turbine, governor, generator and load respectively, and K_{Pi} refers to the load gain in region i . $A_i \in R^{m \times m}$, $B_i \in R^{m \times n}$, $C_{il} \in R^{m \times m}$, $D_i \in R^{m \times k}$ are nominal parameter matrices.

Considering that the system dynamics model contains parameter uncertainty, the corresponding parameter uncertainty terms according to (7) are denoted as ΔA_i , ΔB_i , ΔC_{il} and ΔD_i , and the matrix form of the system with uncertainty is:

$$\begin{aligned} \dot{x}_i(t) &= (A_i + \Delta A_i) x_i(t) + (B_i + \Delta B_i) u_i(t) \\ &+ \sum_{\substack{l \in N \\ l \neq i}} (C_{il} + \Delta C_{il}) x_l(t) + (D_i + \Delta D_i) \Delta P_{Di}(t) \quad (8) \\ &= A_i x_i(t) + B_i u_i(t) + \sum_{\substack{l \in N \\ l \neq i}} C_{il} x_l(t) + \tilde{D}_i(t) \end{aligned}$$

Where

$$\begin{aligned} \tilde{D}_i(t) &= \Delta A_i x_i(t) + \Delta B_i u_i(t) + \sum_{\substack{l \in N \\ l \neq i}} \Delta C_{il} x_l(t) \\ &+ (D_i + \Delta D_i) \Delta P_{Di}(t) \quad (9) \end{aligned}$$

$\tilde{D}_i(t)$ is defined as the set of uncertainties and external disturbances of the system (8). Therefore, $\tilde{D}_i(t)$ is considered to be matched and bounded, i.e.

$$\tilde{D}_i(t) = B_i D'_i(t), \|D'_i(t)\| \leq \delta_1, \|\tilde{D}_i(t)\| \leq \delta_2 \quad (10)$$

Where δ_1, δ_2 are known scalars, $\|\cdot\|$ represents the matrix norm.

For the power system described in (8), the LFC goal is to maintain the stability of the system in the presence of parameter uncertainties and load changes. In the following chapters, integral SMC, improved SMC based on disturbance observer, and IHBA-based control design will be applied to solve this problem.

B. Wind Power Generation Model

Wind turbine is a device that converts wind energy into mechanical energy in nature, mainly including fans, transmissions, generators and other components. First, the kinetic energy of the wind is converted into mechanical energy through the fan, which is an energy capture device. Then, the mechanical energy is increased by acceleration through the gearbox and is transferred to the generator through the transmission. The mechanical energy is converted into electrical energy and then connected to the power grid. During this process, the mechanical output power of the wind turbine is [21]

$$P_{WT} = 0.5 \rho C_p(\lambda, \theta) A_r V_w^3 \quad (11)$$

Where, ρ is the air density; A_r is the swept area of wind turbine blades, V_w is the wind speed before entering the wind turbine, $C_{p(\lambda, \theta)}$ is the wind energy utilization coefficient.

The kinetic energy obtained by wind turbines from nature is limited. According to Bates Theory, the maximum value of the wind energy utilization coefficient is 0.593, and the efficiency of the wind turbine determines the power output of the fan, that is, the wind energy utilization coefficient can be expressed as

$$\begin{aligned} C_p(\lambda, \theta) &= (0.44 - 0.0167\theta) \sin \left[\frac{\pi(\lambda - 3)}{15 - 0.3\theta} \right] \\ &- 0.00184(\lambda - 3)\theta \quad (12) \end{aligned}$$

In (12), θ is the pitch angle, λ is the tip speed ratio, equals to the ratio of wind turbine blade tip speed to wind speed, $\lambda = R\omega_r/V_w$ [22].

According to the relationship between the actual output power P_w of wind power generation and the mechanical power P_{WT} , the actual output power can be obtained as [23]

$$\Delta P_w = \frac{K_{WT}}{1 + sT_{WT}} \Delta P_{WT} \quad (13)$$

In (13), K_{WT} and T_{WT} are the gain and time constant of the wind turbine, respectively.

III. LFC DESIGN

A. Sliding Mode Design

SMC is an effective nonlinear control method. This control strategy can change purposefully and continuously according to the current states of the system such as deviations, integration of deviations and derivatives of deviations in a dynamic process, forcing the system to move along the state trajectory of the predetermined "sliding mode", so as to achieve the control effect. Clearly, it is crucial to design a reasonable sliding mode surface [24, 25], which is obtained by making the designed sliding mode variable zero.

The traditional sliding mode variable can be designed as a linear polynomial of all states of the system. According to each state variable in Fig. 1, the sliding mode surface is designed as follows

$$\sigma_i = G_i x_i(t) = \sum_{j=1}^m g_{ij} x_{ij}(t) \quad (14)$$

Where, $G_i = [g_{i1}, \dots, g_{ij}, \dots, g_{im}]$ is the parameter vector for design, $x_i = [x_{i1}(t), \dots, x_{ij}(t), \dots, x_{im}(t)]^T$ is the state vector of the system. In the system state variables, $\Delta P_{Ei}(t)$ and $\Delta \delta_i(t)$ are the integrals of $ACE_i(t)$ and $\Delta f_i(t)$ respectively. This means that although the deviations are adjusted to zero, their integral state variables are not guaranteed to reach zero at the same time. Therefore, when the traditional sliding mode variables are used for frequency adjustment, the system frequency $f_i(t)$ will have a steady-state error and deviate from the expected value.

On the basis of the traditional sliding mode surface designed, aiming at the integral effect problem, an integral-type sliding mode surface is selected to improve the dynamic performance and robustness of the matching disturbance in the arrival stage. The improved sliding mode surface is designed as follows

$$\tilde{\sigma}_i(t) = \sigma_i(t) - \int_0^t G_i (A_i - B_i L_i) x_i(\tau) d\tau \quad (15)$$

Where, L_i is a constant matrix. Obviously, $G_i B_i$ is non-singular, L_i is chosen by pole configuration such that $\lambda(A - B_i L_i) < 0$.

According to the designed reaching law and sliding mode variables, the corresponding sliding mode control law is derived. In order to ensure that the reachable condition of the designed sliding surface $\tilde{\sigma}_i(t)$ is established, that is $\sigma_i(t) \dot{\sigma}_i(t) < 0$, the reach condition can be designed as

$$\dot{\tilde{\sigma}}_i(t) = -\kappa_i \tilde{\sigma}_i(t) - \eta_i \operatorname{sgn}(\tilde{\sigma}_i(t)) \quad (16)$$

Where, $-\kappa_i \tilde{\sigma}_i(t)$ is the exponential approach term, $-\eta_i \operatorname{sgn}(\tilde{\sigma}_i(t))$ is the isokinetic approach term, the approach law can ensure that the moving point arrives in a limited time.

To reduce chattering and provide a continuous control signal, a saturation function is used in the ideal sliding mode to replace the sign function

$$\operatorname{sat}(\tilde{\sigma}_i(t)) = \begin{cases} \operatorname{sign}(\tilde{\sigma}_i(t)) & \text{if } \|\tilde{\sigma}_i(t)\| > \Delta \\ k\tilde{\sigma}_i(t) & \text{if } \|\tilde{\sigma}_i(t)\| \leq \Delta, k = \frac{1}{\Delta} \end{cases} \quad (17)$$

Where, Δ represents the thickness of the boundary layer of the saturation function. Outside the boundary layer, switching control is adopted, while linearization feedback control is used inside the boundary layer.

According to (14)-(17), the sliding mode control output can be obtained as

$$u = -L_i x_i - (G_i B_i)^{-1} \left[G_i \tilde{D}_i(t) + G_i \sum_{\substack{l \in N \\ l \neq i}} C_{il} x_l(t) + \kappa_i \tilde{\sigma}_i(t) + \eta_i \operatorname{sat}(\tilde{\sigma}_i(t)) \right] \quad (18)$$

Since the disturbance $\tilde{D}_i(t)$ is unknown, according to (10), the traditional sliding mode controller requires $|\tilde{D}_i(t)| < \delta_i$, and the boundary value δ_i is used to replace the actual load disturbance value. Alternatively, the disturbance term is usually not introduced in the sliding mode surface design, which is the robustness feature of sliding mode control. Obviously, such a control design is inaccurate. Therefore, this paper introduces a disturbance observer to estimate $\tilde{D}_i(t)$, so as to improve the control accuracy.

B. SMC Design Based on Disturbance Observer

The system of (8) is simplified as

$$\dot{x} = Ax(t) + Bu(t) + \tilde{C}x_i(t) + \tilde{D}(t) \quad (19)$$

$\tilde{D}(t)$ represents the lumped disturbance in a single region of the system. For the nonlinear disturbance observer [26], the disturbance in (19) can be estimated, represented by (20)

$$\dot{\hat{D}} = -l(x)\hat{D}(x) + l(x) \left[\dot{x} - Ax - Bu - \tilde{C}x_i \right] \quad (20)$$

Where, $l(x)$ is the gain of the disturbance observer, \hat{D} is the estimated lumped disturbance of the system.

The basic disturbance observer requires the derivative of the state variables, which couldn't be measured directly and can cause noise amplification in the state variables during the derivation process. Therefore, according to the literature [27], an intermediate variable $z = \hat{D} - p(x)$ is introduced to improve the disturbance observer, and the improved disturbance observer can be expressed as

$$\begin{cases} \dot{z} = -l(x)z - l(x) \left[Ax + Bu + \tilde{C}x_i + p(x) \right] \\ \hat{D} = z + p(x) \end{cases} \quad (21)$$

Where, z is the intermediate variable of the observer, $p(x)$ is the designed nonlinear function, and the relationship between the observer gain and it is as follows

$$l(x) = \frac{\partial p(x)}{\partial x} \quad (22)$$

Theorem 1: Considering that the system selects a proper nonlinear gain function, the disturbance observer (21) can exponentially track the disturbance, as follows

$$\dot{e}_d(t) = -l(x)e_d(t) \quad (23)$$

Where, e_d is the estimated disturbance error. It is easy to see that when the error is dynamic and stable, the error of the disturbance observer will tend to zero and has nothing to do with the state variables.

Proof: When the disturbance changes slowly, its derivative is easy to be zero. Combining (19) and (21)-(23), we can get

$$\begin{aligned} \dot{e}_d &= \dot{\tilde{D}} - \dot{\hat{D}} \\ &= -\left(\dot{z} + \frac{\partial p}{\partial x} \dot{x}\right) \\ &= -l(x)z - l(x)\left[Ax + Bu + \tilde{C}x_i + p(x)\right] \\ &\quad + l(x)\left(Ax + Bu + \tilde{C}x_i + \tilde{D}\right) \\ &= -l(x)\left(\tilde{D} - \hat{D}\right) = -l(x)e_d \end{aligned}$$

In order to improve the precision of the designed sliding mode control, on the basis of the disturbance estimation of (21), the sliding mode surface of the system is redesigned when there is concentrated disturbance, and the expected disturbance of the system will eventually approach zero. So the estimated disturbance value is introduced into the sliding mode control variable, as follows

$$\tilde{\sigma}_i(t) = \sigma_i(t) - \int_0^t G_i(A_i - B_i L_i)x_i(\tau) d\tau + \hat{D} \quad (24)$$

Based on the sliding mode surface of (25) and the observer of (21), the redesigned sliding mode control output can be obtained as

$$u = -L_i x_i - (G_i B_i)^{-1} \left[G_i \hat{D}_i(t) + G_i \sum_{\substack{l \in N \\ l \neq i}} C_{il} x_l(t) + \kappa_i \tilde{\sigma}_i(t) + \eta_i \operatorname{sgn}(\tilde{\sigma}_i(t)) \right] \quad (25)$$

Where, η_i is the designed switching gain, so that the system state can reach the switching surface, and η_i satisfies the following conditions

$$\eta_i \geq (G_i + l(x))e_d \quad (26)$$

The block diagram of the realization of SMC based on the disturbance observer is shown in Fig. 2. The designed disturbance observer is suitable for general uncertainty power systems. Furthermore, the observer and controller can be designed separately.

Theorem 2: If the switching gain satisfies (26), and the disturbance observer (21) selects a suitable nonlinear gain, then the closed-loop system (8) based on the proposed control law (25) is asymptotically stable.

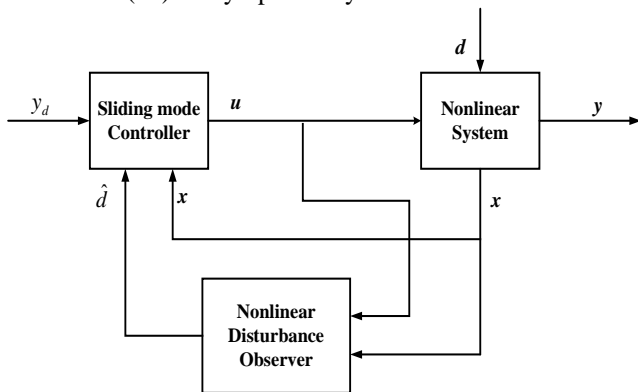


Fig. 2. Structure of disturbance observer based on sliding-mode control

Proof: Defining the Lyapunov Function

$$V(t) = \frac{1}{2} \tilde{\sigma}_i^2(t) \quad (27)$$

The derivative of the sliding surface function is

$$\dot{\tilde{\sigma}}_i(t) = G_i \dot{x}_i(t) - (G_i A_i - G_i B_i L_i) x_i(t) + \dot{\hat{D}} \quad (28)$$

Taking the control law (25) and (8) into (28), we get

$$\dot{\tilde{\sigma}}_i(t) = -\kappa_i \tilde{\sigma}_i(t) - \eta_i \operatorname{sgn}(\tilde{\sigma}_i(t)) + \dot{\hat{D}} \quad (29)$$

Where, $\tilde{\sigma}_i(t)$ is the sliding mode surface. Taking (21) and (29) into (27), the derivative of $V(t)$ is as follows

$$\begin{aligned} \dot{V}(t) &= \tilde{\sigma}_i(t) \dot{\tilde{\sigma}}_i(t) \\ &= \tilde{\sigma}_i(t) \left[-\kappa_i \tilde{\sigma}_i(t) - \eta_i \operatorname{sgn}(\tilde{\sigma}_i(t)) + \dot{\hat{D}} \right] \\ &= \tilde{\sigma}_i(t) \left[(G_i + l(x))(\tilde{D}_i - \hat{D}_i) - \kappa_i \tilde{\sigma}_i(t) - \eta_i \operatorname{sgn}(\tilde{\sigma}_i(t)) \right] \\ &= \tilde{\sigma}_i(t) (G_i + l(x)) e_d - \kappa_i \tilde{\sigma}_i^2(t) - \eta_i \tilde{\sigma}_i \operatorname{sgn}(\tilde{\sigma}_i(t)) \\ &\leq -|\tilde{\sigma}_i(t)| \left[\eta_i - (G_i + l(x)) e_d \right] - \kappa_i \tilde{\sigma}_i^2(t) \end{aligned}$$

Obviously, under the given condition (26), $\dot{V} < 0$, the system under the reconstructed sliding mode controller based on the observer is asymptotically stable, and the system states can asymptotically approach the desired value. That is, it can suppress the frequency deviation caused by the disturbance and realize the stability of the power system.

C. IHBA-Based SMC Design

i) Standard HBA

The Honey Badger Algorithm [28] is a new meta-heuristic algorithm proposed by Fatma A. Hashima et al. in 2021. The optimal solution was found by simulating the foraging behavior of the two modes of honey badger. Due to its good experimental performance and simple structure, this algorithm is selected to optimize the controller parameters. The specific steps of the algorithm are as follows.

Step 1: Initialize

Initialize the position of each honey badger in a given population according to (30)

$$m_k = lb_k + r_1 \times (ub_k - lb_k), r_1 \in [0, 1] \quad (30)$$

Where, m_k is the position of the k -th honey badger in the honey badger population, and ub_k and lb_k are the upper and lower bounds of the given search space, respectively.

Step 2: Define the target odor intensity (I_k)

The intensity of the scent is related to the distance between individual honey badgers and the distance between the honey badger and the target. The higher the target odor intensity, the faster the honey badger moves. Odor intensity is defined as follows

$$I_k = r_2 \times \frac{L}{4\pi s_k^2} \quad (31)$$

$$L = (m_k - m_{k+1})^2 \quad (32)$$

$$s_k = m_{prey} - m_k \quad (33)$$

Where, s_k is the distance between the honey badger and the target, L is the source strength.

Step 3: Refresh the density factor (λ)

In order to achieve a smooth transition between exploration and production, a density coefficient is used to control the time-varying randomization. The density coefficient update decreases with the number of iterations, as in (34)

$$\lambda = \beta \times \exp\left(-\frac{t}{t_{\max}}\right) \quad (34)$$

Where, β is a constant, $\beta \geq 1$ (default = 2).

Step 4: Avoid local optima

During algorithm position update phase, the flag F is used to change the direction of the search, so that the agent can scan the search space more fully to avoid local optima.

Step 5: Update the proxy location

The algorithm sets two location update modes, namely digging phase and honey phase. In the excavation stage, the honey badger moves in a cardioid-like diagram, and the position update equation in this stage is expressed as

$$m_{new} = m_{prey} + F \times \alpha \times I \times m_{prey} + F \times r_3 \times \lambda \times s_k \times \left| \cos(2\pi r_4) \times [1 - \cos(2\pi r_5)] \right| \quad (35)$$

Where, m_{prey} represents the best position found so far, that is, the position of the prey, α represents the ability of the honey badger to catch prey, $\alpha \geq 1$, the default is 6. r_3, r_4, r_5 are unequal random numbers, and the range is 0 to 1.

In the honey stage, the honey badger follows the guide bird to the hive, and the behavior of hitting the hive is simulated as the following formula.

$$m_{new} = m_{prey} + F \times r_7 \times \lambda \times s_k \quad (36)$$

Where, s_k represents the distance between the honey badger and the hive, and search is performed near the currently found target m_{prey} . The search behavior at this stage is affected by the density coefficient λ .

ii) Improved HBA

The original Honey Badger algorithm is able to provide good results for parameter optimization problems. However, it can lead to inappropriate results in some cases due to premature convergence or trapping in local optima. In order to better balance the search performance of the algorithm, a series of improved methods have been proposed [29, 30]. In view of the shortcomings of standard HBA, we propose three improvement methods.

(i) Inertia weight

Introduce inertia weight [31] w in honey badger digging stage and honey stage to enhance the local search ability of honey badger.

$$\begin{cases} m_{new} = w(t-1) \times m_{prey} + F \times \alpha \times I \times m_{prey} \\ \quad + F \times r_3 \times \lambda \times s_k \times \left| \cos(2\pi r_4) \times [1 - \cos(2\pi r_5)] \right| \\ m_{new} = w(t-1) \times m_{prey} + F \times r_7 \times \lambda \times s_k \end{cases} \quad (37)$$

The weight w expression is as follows

$$w(t) = w_{max} + (w_{max} - w_{min}) \times \exp\left(-25 \times \left(\frac{t}{t_{max}}\right)^3\right) \quad (38)$$

Where, w_{max} and w_{min} represent the upper and lower bounds of the inertia weight introduced, which are 0.9 and 0.3. t represents the current number of iterations, and t_{max} represents the maximum number of iterations.

(ii) Mirror population selection

The mirror selection strategy is a method to make the population undergo mirror mutation, which can perform directional mutation operation on the population after each iteration, thereby enhancing the diversity of the population. This strategy improves the efficiency and accuracy of algorithm optimization by extracting the optimal individuals to form a new population. The variation formula is as follows

$$m'_k(t) = ub + lb - m_k(t) \quad (39)$$

Where, m_k refers to the k -th individual after the t -th iteration, ub and lb represent the upper and lower bounds of the given search space, respectively, and m'_k refers to the individual generated after mirror mutation.

Then, the individuals generated by the mirror mutation are merged with the original population individuals. At this time, the number of populations is twice the original, and the fitness value of each individual is calculated separately. Eventually, the first N individuals are selected as the population of the next iteration according to the fitness value sorting.

(iii) Levy flight strategy

The Levy flight strategy [32] is a random search method that obeys the Levy distribution. When the particle cannot improve its own solution within a limited time, the Levy flight method is used to redistribute within a given search domain. This improves the diversity of the algorithm population and avoids falling into local optimum. After introducing the Levy flight strategy, the position update formula is as follows (40)

$$m_k^{(t+1)} = m_k^{(t)} + S_{Levy} \cdot randn(0,1) \quad (40)$$

Where, $m_k^{(t+1)}$ is the position of k -th honey badger in the t -th iteration of the algorithm, and S_{Levy} is the step size of Levy's flight. The specific expression is as follows

$$\begin{cases} S_{Levy}(\tau) \sim \frac{u}{|v|^{\frac{1}{\tau}}} \\ \zeta = \left(\frac{\Gamma(1+\tau) \times \sin\left(\frac{\pi\tau}{2}\right)}{\Gamma\left(\frac{1+\tau}{2}\right) \times \tau \times 2^{\frac{\tau-1}{2}}}\right)^{\frac{1}{\tau}} \end{cases} \quad (41)$$

Where, u and v follow a normal distribution, Γ follows the standard Gamma distribution, τ is a constant index, $\tau \in (0,2]$.

The specific flow chart of the IHBA algorithm is shown in Fig. 3.

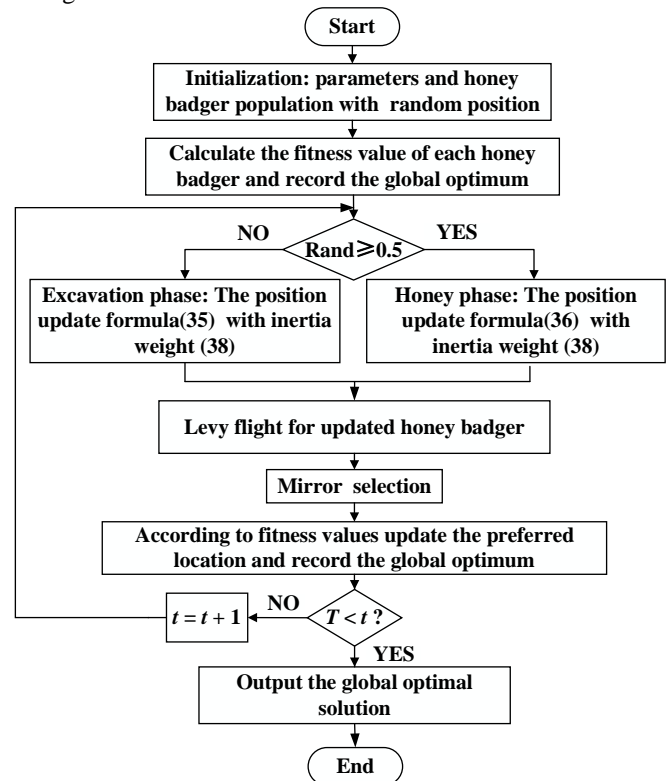


Fig. 3. The flow chart of IHBA algorithm

For the multi-region interconnected power system, the designed sliding mode controller has the adjustable parameters κ_i , η_i and $\{g_{ij}\}$. Given the parameter search space and the selected objective function, the IHBA algorithm is used to adjust the required parameters of the controller.

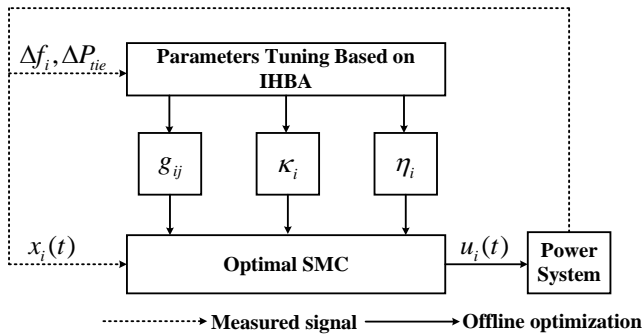


Fig. 4. Schematic diagram of the IHBA-based SMC method

The search performance of meta-heuristic algorithms such as IHBA depends to a large extent on the setting of the fitness function [19, 33-35]. In the design of the LFC model, the parameters measured and adjusted are mainly the frequency deviation (ΔF) of the power system and the tie-line power deviation (ΔP_{tie}). Therefore, in the optimization of controller parameters, four performance indicators, ITAE, ITSE, ISE, and IAE are usually used [36]. According to the research and design experience of related work, this study uses the performance indicator ITSE as the fitness function, as follows.

$$J = ITSE = \int_0^{t_{sim}} t \cdot \left(|\Delta f_i|^2 + |P_{tie,i-j}|^2 \right) dt \quad (42)$$

System frequency deviation and tie-line power deviation are input signals for calculating fitness value. The smaller the fitness value is, the smaller the frequency deviation of the power system is, and the better the control performance is. According to the design experience gained from simulation studies, the search range for setting these parameters is $g_{ij} \in [0, 20]$, $\kappa_i \in [0, 20]$, $\eta_i \in [0, 15]$. The user-defined parameters in the algorithm are all default values. For the two-region power interconnection system, the parameter size that needs to be optimized by the algorithm is $m+2$, which is 7 (assuming that the same parameters are used for the sliding-mode controllers in each region). For the three-region power interconnection system, the particle size is 21. The SMC control method based on the IHBA algorithm is shown in Fig. 4.

IV. RESULTS AND DISCUSSIONS

A. Standard functions

In order to objectively verify the effectiveness of the proposed strategies to improve the honey badger algorithm, four benchmark functions are introduced to test the performance of the proposed IHBA algorithm against a series of standard algorithms.

As shown in TABLE I, the four test functions are all single-objective test functions, including multi-modal function and unimodal function, which are comprehensive enough to explore the performance of the algorithm in different scenarios. The dimension of all test functions is set to 30, the population size is set to 50, and the maximum

number of iterations is set as follows: $f_1(x)$ and $f_2(x)$ are set to 3000 times, $f_3(x)$ and $f_4(x)$ are set to 1500 times, and the algorithm simulation experiment is repeated for 30 times.

TABLE I
FOUR STANDARD TEST FUNCTIONS

F	Expression	Ranges
Step Function (f_1)	$f_1(x) = \sum_{i=1}^D ([x_i + 0.5])^2$	$[-100, 100]^D$
Quartic Function i.e. Noise (f_2)	$f_2(x) = \sum_{i=1}^D ix_i^4 + \text{random}[0, 1)$	$[-10, 10]^D$
Generalized Schwefel's Problem 2.26 (f_3)	$f_3(x) = -\sum_{i=1}^D x_i \sin(\sqrt{ x_i })$	$[-500, 500]^D$
Generalized Penalized Function No.02 (f_4)	$f_4(x) = 0.1 \left\{ \sin^2(\pi 3x_1) + \sum_{i=1}^D (x_i - 1)^2 \right. \\ \left. [1 + \sin^2(3\pi x_{i+1})] + (x_D - 1)^2 [1 + \sin^2(2\pi x_D)] \right\} + \sum_{i=1}^D u(x_i, 5, 100, 4)$	$[-50, 50]^D$

TABLE II
RESULTS OF TEST FUNCTIONS UNDER DIFFERENT ALGORITHMS

F		PSO	WOA	HBA	IHBA
f_1	MEAN	5.64E-08	1.10E-03	3.11E-10	5.90E-12
	STDEV	3.24E-09	7.84E-04	1.56E-10	1.18E-11
	BEST	2.18E-09	6.07E-04	1.29E-10	3.05E-15
	WORST	1.00E-08	2.50E-03	4.63E-10	2.70E-11
f_2	MEAN	9.20E-03	8.89E-03	4.05E-04	2.67E-05
	STDEV	2.90E-03	8.03E-03	3.78E-04	2.85E-05
	WORST	1.25E-02	2.10E-02	1.10E-03	7.49E-05
f_3	MEAN	-7.75E+03	-7.80E+03	-8.20E+03	-1.01E+04
	STDEV	4.54E+02	5.24E+02	3.67E+02	9.36E+02
	BEST	-8.13E+03	-8.40E+03	-8.54E+03	-1.12E+04
f_4	WORST	-7.02E+03	-7.09E+03	-7.66E+03	-8.68E+03
	MEAN	2.20E-03	6.73E-02	7.83E-04	4.10E-04
	STDEV	4.90E-03	1.14E-01	1.10E-03	5.30E-04
	BEST	1.14E-08	1.90E-03	1.01E-09	5.08E-15
	WORST	1.10E-02	2.70E-01	2.40E-03	2.50E-03

Fig. 5-8 show the convergence curves of IHBA and HBA in the four test functions. It can be seen that after introducing the three improvement strategies, the optimization ability of HBA is enhanced, which leads to higher optimization accuracy and faster convergence. At the same time, compared to HBA, IHBA reduces the probability of falling into a local optimum and enhances the ability to find a global optimal solution.

In order to further strengthen the explanatory power and comparability of the experimental results, PSO and WOA algorithms are introduced as the control experimental groups. The average value, standard deviation, best value and worst value of each algorithm in different test functions are recorded. The results in TABLE II show that the performance of the improved HBA algorithm is better than that of the standard HBA in both single-peak and multi-peak test functions. At the same time, it can also be seen that HBA has a stronger optimization capability compared to the other algorithms.

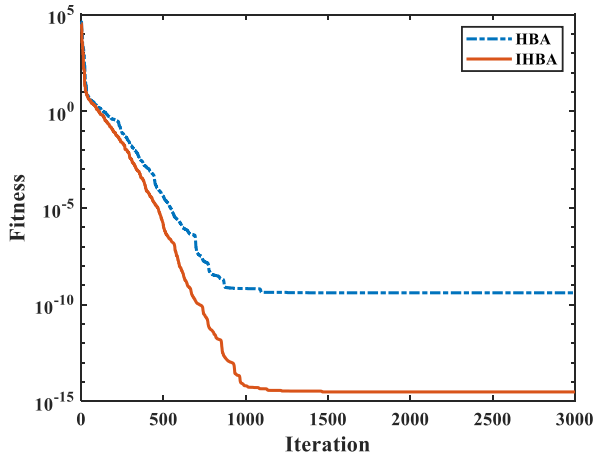


Fig. 5. Convergence curves of different algorithms on $f_1(x)$

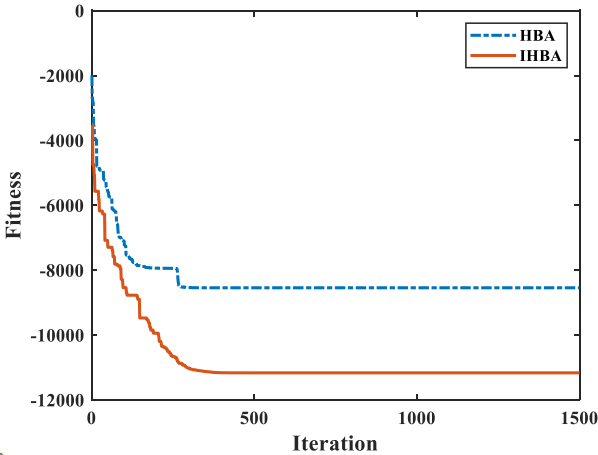


Fig. 7. Convergence curves of different algorithms on $f_3(x)$

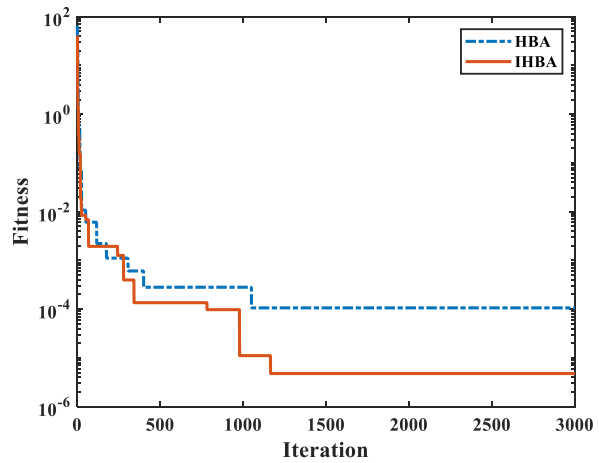


Fig. 6. Convergence curves of different algorithms on $f_2(x)$

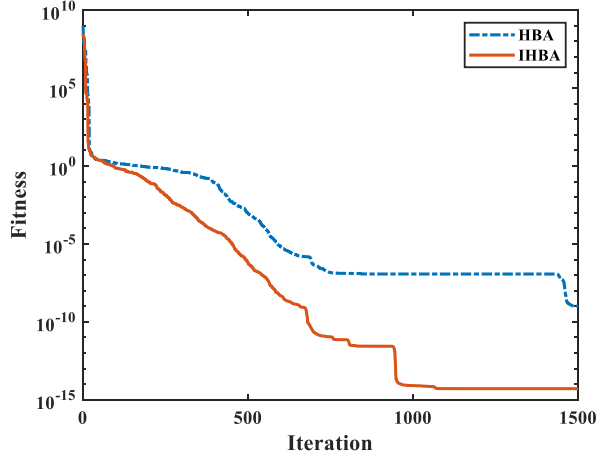


Fig. 8. Convergence curves of different algorithms on $f_4(x)$

B. Two-area non-reheat thermal system

In this section, simulation studies are carried out in the MATLAB(R2020b)/Simulink environment to investigate the performance of the proposed control method. The parameters of the system and the detailed dynamic models are found in Appendix.

First, the simulation test is performed using the two-region power system shown in Fig. 12 with the parameters given in Appendix A. In order to investigate the superiority of the proposed IHBA-optimized DOSMC control strategy, it is compared with the standard HBA algorithm-optimized PID controller and the standard HBA algorithm-optimized DOSMC controller. A step load change with a perturbation of 10% is applied at $t=1s$ in area-1. During the optimization

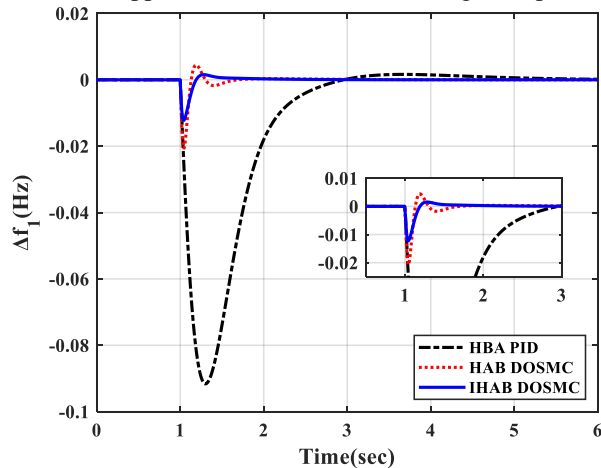


Fig. 9. Frequency deviation of area-1 due to 10% step disturbance in area-1

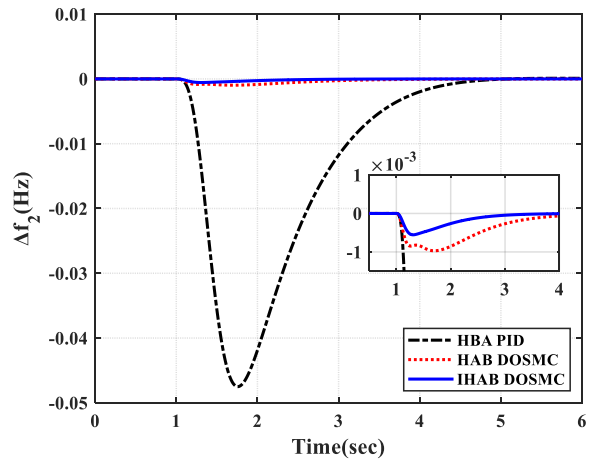


Fig. 10. Frequency deviation of area-2 due to 10% step disturbance in area-1

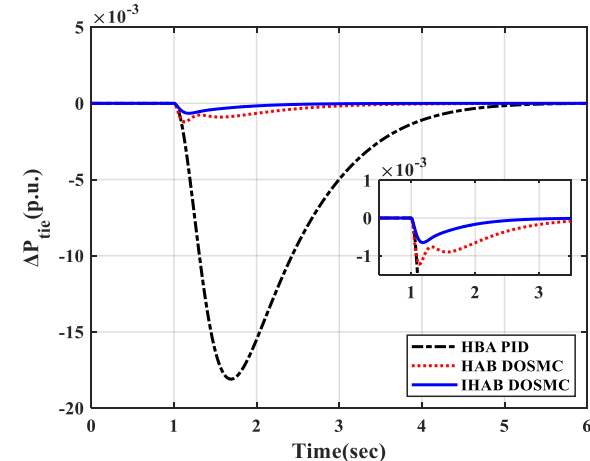


Fig. 11. Tie-line power deviation due to 10% step disturbance in area-1

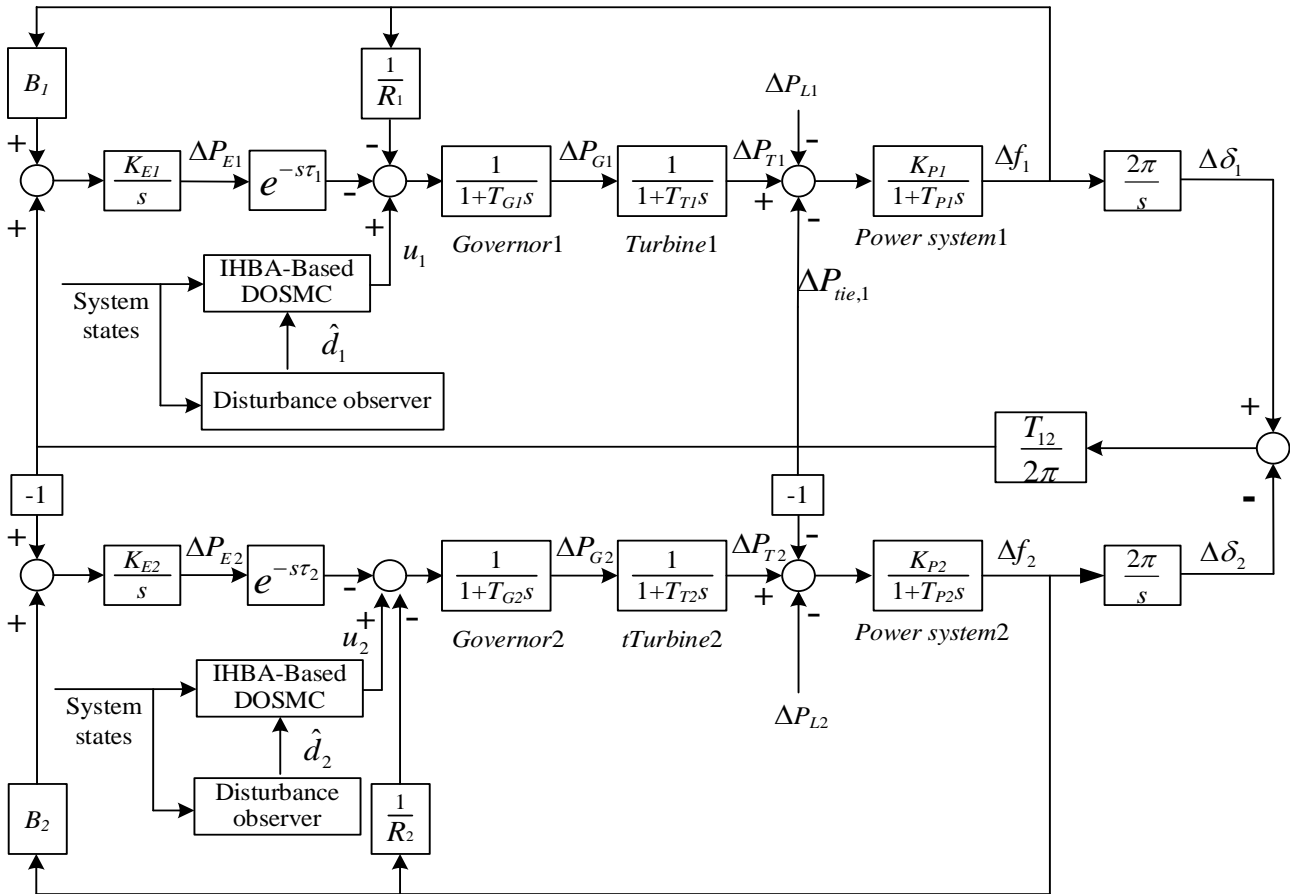


Fig. 12. Transfer function model of two-area power system with delay

TABLE III
OPTIMUM CONTROLLER PARAMETERS OF PID/DOSMC BASED ON HBA/IHBA

	Parameter values						
HBA PID	K_{p1}	K_{i1}	K_{d1}	K_{p2}	K_{i2}	K_{d2}	-
	1.1905	1.9841	0.4960	1.0913	0.4960	0.9921	-
	g_{i1}	g_{i2}	g_{i3}	g_{i4}	g_{i5}	κ_i	η_i
HBA DOSMC	5.1516	10.7487	0.0290	10.5940	4.7849	10.5940	5.7915
IHBA DOSMC	8.7379	3.4647	0.0481	6.2264	14.2343	1.1846	11.9103

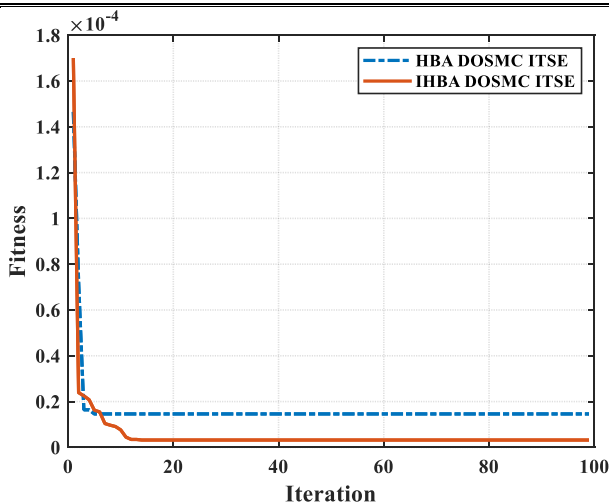


Fig. 13. Fitness value of HBA/IHBA due to 10% step disturbance in area-1

process, the same criterion ITSE is used to adjust the controller parameters. 30 independent simulations were carried out respectively, and the optimal group was selected from the results as the parameters of various control methods. The specific data are shown in TABLE III. The

regional frequency, the deviation of the tie line power and the response curve of the objective function are shown in Fig. 9-11 and Fig. 13.

It can be seen from the figures: i) Compared with the traditional PID controller, the proposed DOSMC has a stronger damping effect on frequency fluctuations when the power system load changes, and can provide faster feedback compensation, showing a better adjustment effect. ii) The IHBA-optimized DOSMC controller can achieve better dynamic performance, with Δf_i and ΔP_{12} exhibiting lower undershoot, lower overshoot, and smaller oscillations.

In addition, to verify the optimized performance of IHBA and HBA, the fitness values of IHBA and HBA under the same criterion of ITSE are tested for the proposed control method under a 10% load disturbance in region 1. The iteration curve is shown in Fig. 13. It can be seen from the graph analysis that IHBA effectively balances the local search and global search capabilities, and improves the accuracy of search results, which proves that IHBA has better parameter optimization capabilities. Therefore, it can be proved that the IHBA-optimized DOSMC is effective in improving the control performance.

Case A: Step Change

To further demonstrate the superiority of the system dynamic performance under the proposed strategy, the system is tested under three different step load perturbation (SLP) conditions. The results are compared with traditional PID controller optimized by BFOA [16], FPI optimized by hybrid PSO-PS [37], and fuzzy PID optimized by hybrid HS-COA [38], respectively. In addition, to verify the effectiveness of the sliding mode controller reconstruction based on the disturbance observer, the SMC term without the observer is introduced for comparison. The evaluation

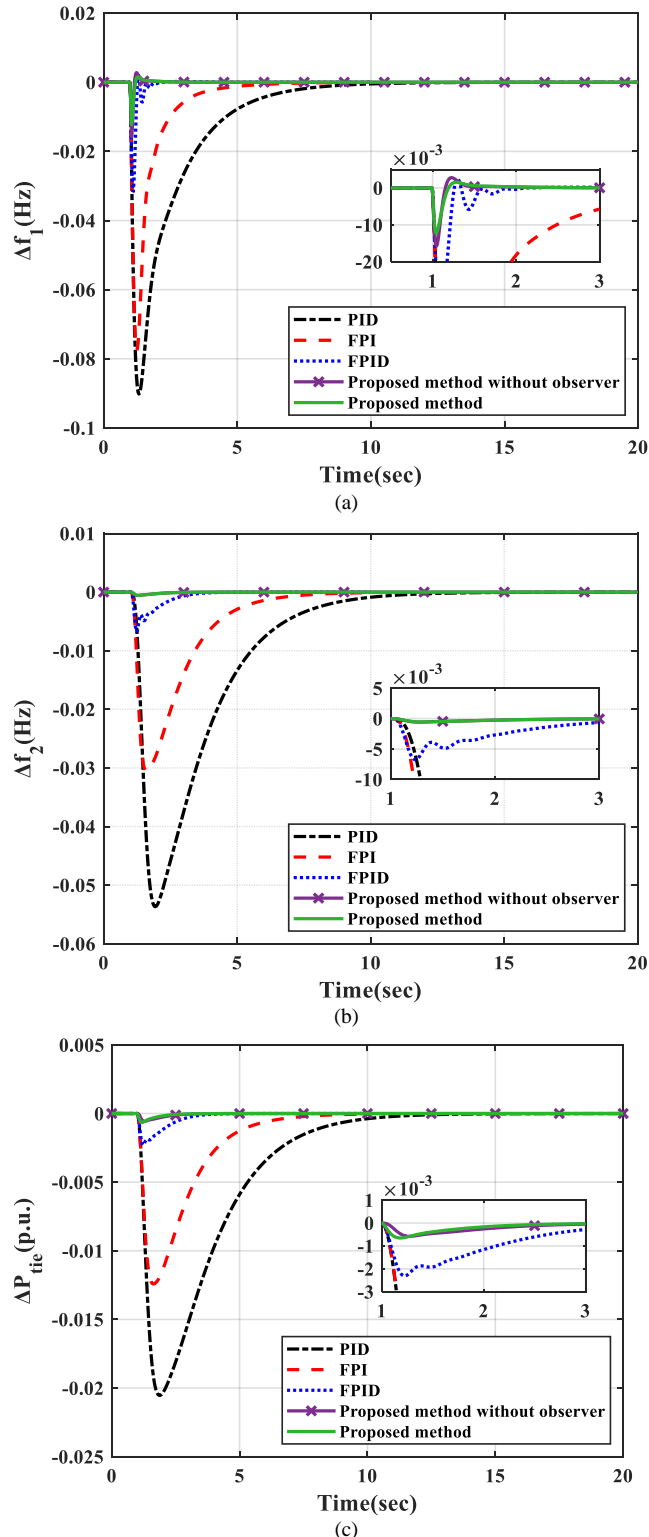


Fig. 14. Deviations of different controllers for Case1. (a) Frequency deviation of area-1. (b) Frequency deviation of area-2. (c) Tie-line power deviation.

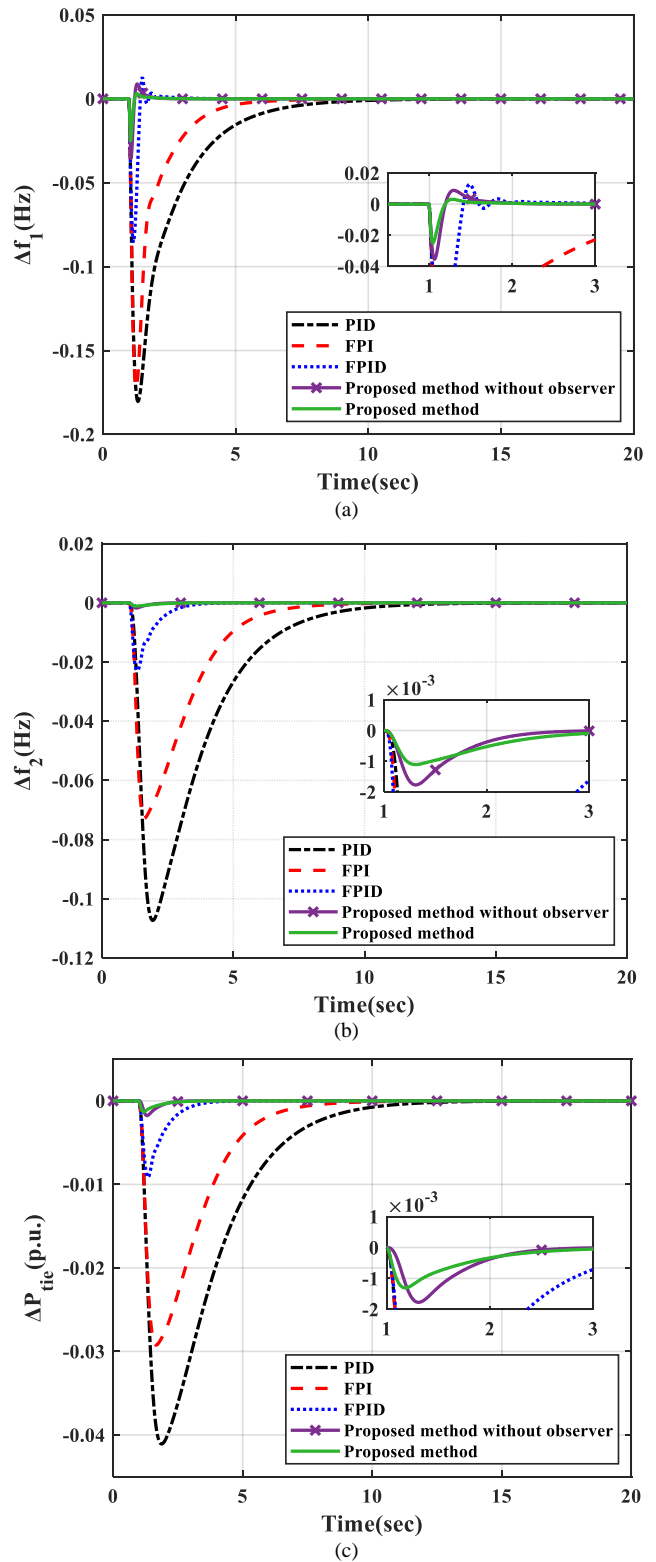


Fig. 15. Deviations of different controllers for Case2. (a) Frequency deviation of area-1. (b) Frequency deviation of area-2. (c) Tie-line power deviation.

metrics consist of the dynamic indicators T_s , US , OS , E_{ss} and performance indicators ITSE, which are computed dynamically based to the frequency response of the system. The detailed data is presented in TABLE IV.

(i) Case1: Area-1 has a 10% step load change

At $t=1s$, there is a 10% load demand change in area-1. Fig. 14 shows the frequency response curves of the power system under three control strategies, including the SMC control method with or without disturbance observer

optimized based on IHBA algorithm, and PID, FPI, FPID control strategies. It is easy to see from the figure that the proposed control strategy exhibits a better dynamic response in the presence of load variation compared to other control strategies. At the same time, the SMC reconstruction based on the perturbed observer has better control accuracy, which allows the region-1 with larger disturbance to adjust the frequency with smaller overshoot fluctuations and faster velocity, and the system performs better dynamically under this strategy. From the quantitative analysis of the data in the TABLE IV, it can be seen that the performance indicators of the proposed control strategy, such as objective function, overshoot and adjustment time, are better than other control methods. The results show that the dynamic performance and stability of the system is better under this control strategy. Moreover, the improved strategy of reconstructing the SMC based on the disturbance observer is beneficial to improve the performance of the controller.

(ii) *Case2*: Area-1 has a 20% step load change

On the basis of case 1, case2 doubles the load variation in area-1, so the performance metrics in each area of the system decrease and the objective function values, OS and T_s increased significantly. The results in Fig. 15 and TABLE IV show that the performance of the proposed control strategy is more stable than other control methods. Although the disturbance is more severe, the performance indicators do not decrease significantly with the increasing load and are all within acceptable ranges.

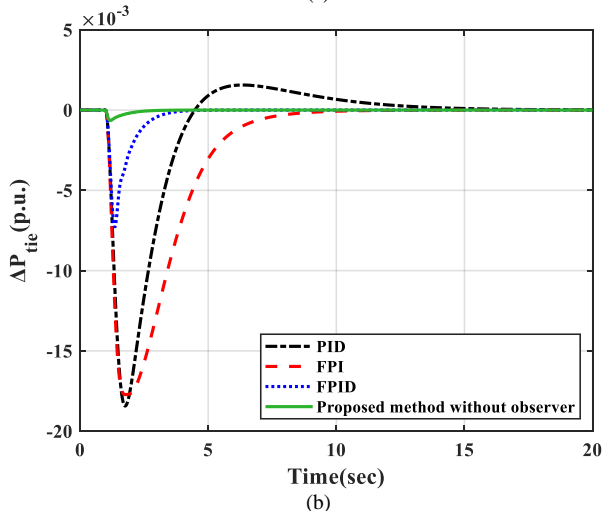
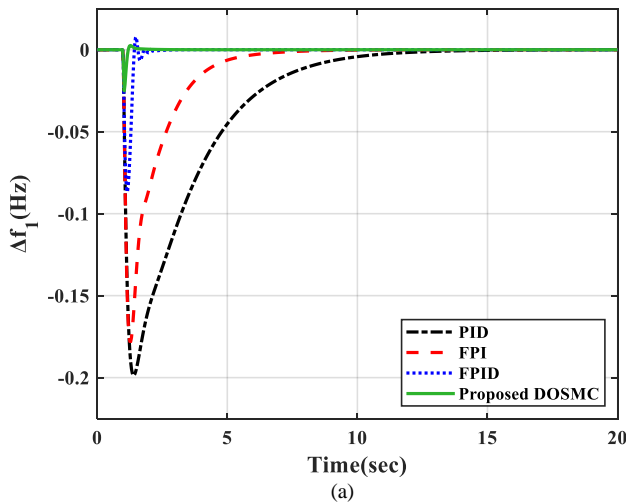


Fig. 16. Deviations of different controllers for *Case3*. (a) Frequency deviation of area-1. (b) Tie-line power deviation.

(iii) *Case3*: Step load change in two areas

Considering the load change in each area, at $t=1s$, a 20% load disturbance is applied to area-1 and a 10% load disturbance is applied to area-2, respectively. The frequency response curve of the system is shown in Fig. 16, and the relevant performance indicators are shown in TABLE IV. Compared with case1 and case2, the overshoot and adjustment time of the frequency response of case3 are larger. As shown in the figure and table, various performance indicators of the system under other control strategies have changed significantly, while the performance indicators of the system based on the proposed control strategy are excellent. Although the location and magnitude of the load disturbance changes, the power system under this control strategy still has better stability compared to other control strategies, thus reflecting the superiority of the proposed control approach.

Case B: Robustness study

In order to study the robustness of the proposed controller, the Absolute Maximum Deviation (AMD) of the two-region frequency and the tie-line power deviation of the proposed controller are compared with those of the PID, FPI, and FPID controllers. To do this, random load perturbations are applied to the loads in these two regions. The random load change is set as a step change randomly distributed between $-0.2p.u. \sim 0.2p.u.$ with an average amplitude of $\pm 0.1p.u.$, the sampling frequency of the load change in area-1 is set as 0.01, and the sampling frequency in area-2 is set as 0.1. The results of different control strategies are compared in Fig. 17. Under the same random load variation, the AMD data fluctuation range of the proposed controller is the smallest. Boxplots show that the proposed controller has better robustness compared to other control methods. Furthermore, the proposed control strategy provides a smaller median value.

Case C: Sensitivity to Parameter Uncertainty

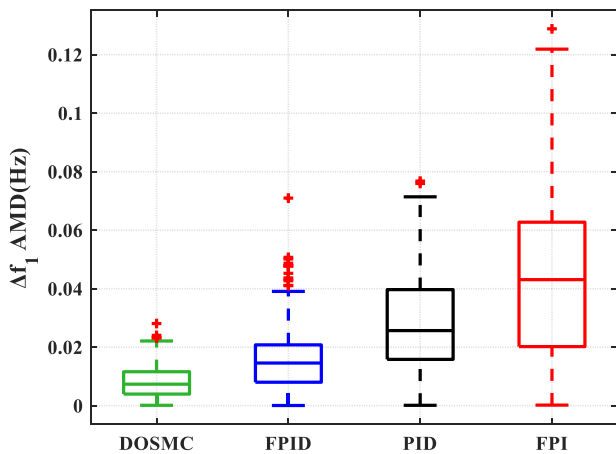
In order to further test the robustness of the proposed controller, uncertainties are introduced into the system model parameters and load conditions to conduct system sensitivity analysis. Therefore, the uncertainties of the system are simulated by changing the parameters of the load and the controlled system ($Load, T_G, T_T, T_{12}$) with the controller parameters unchanged. Fig. 18 and Fig. 19 show the fluctuation of the system caused by the change of system parameters, and TABLE V lists the performance indicators under different conditions.

(i) Load change

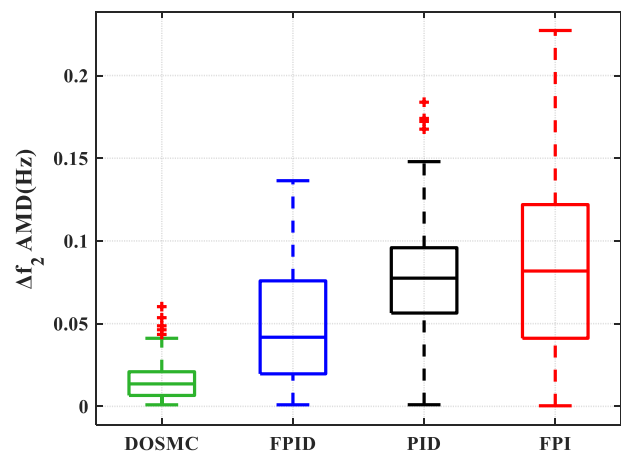
By changing the load conditions, the robustness of the system to a wide range of load changes is studied. At $t=1s$, the SLP of area-1 is 1%. The load in area-1 varies within $\pm 50%$ of the nominal value, and the dynamic response of the system under varying load conditions is shown in Fig. 18. It can be seen from the figure that the five curves under different load conditions basically overlap, and the system can quickly respond to the load change and adjust to a stable state. Undershoot and overshoot vary with the magnitude of the disturbance to a certain extent, while the change in the adjustment time is small. It is easy to see from the data recorded in TABLE V that the performance indicators before and after the load change can be maintained within a

TABLE IV
PERFORMANCE COMPARISON OF TWO-AREA SYSTEM WITH DIFFERENT CONTROL METHODS

Index		BFOA PID[16]	hPSO-PS FPI[37]	HSCOA FPID[38]	IHBA SMC	IHBA DOSMC		
Case1	$T_s(s)$ (± 0.0005)	Δf_1	9.9484	6.3687	1.8222	1.8612	1.6239	
		Δf_2	11.0389	7.5392	3.1616	1.6070	1.4646	
		ΔP_{tie}	9.4994	6.2821	2.6308	1.4334	1.3480	
	US	Δf_1	-0.0902	-0.0774	-0.0317	-0.0178	-0.0123	
		Δf_2	-0.0537	-0.0304	-0.0068	-0.0008	-0.0006	
		ΔP_{tie}	-0.0205	-0.0124	-0.0023	-0.0011	-0.0007	
	OS	Δf_1	0.0000	0.0000	0.0025	0.0044	0.0015	
		Δf_2	0.0000	0.0000	1.07E-07	8.92E-07	2.42E-14	
		ΔP_{tie}	0.0000	0.0000	1.14E-07	1.10E-06	4.73E-15	
	Ess	Δf_1	-2.88E-06	-4.91E-05	-1.57E-09	-1.88E-15	-4.69E-15	
		Δf_2	-4.09E-06	-9.88E-05	1.82E-09	4.75E-15	-5.8E-15	
		ΔP_{tie}	-1.07E-06	-4.12E-05	7.99E-10	2.16E-15	2.88E-15	
	ITSE		0.0687	0.0139	0.0003	4.32E-05	1.62E-05	
	Case2	$T_s(s)$ (± 0.0005)	Δf_1	11.2661	7.9115	3.1184	2.0643	2.0633
			Δf_2	12.3204	9.0552	3.6753	1.8946	2.0315
ΔP_{tie}			10.7219	7.7831	3.2032	1.6503	1.7670	
US		Δf_1	-0.1804	-0.1722	-0.0855	-0.0355	-0.0250	
		Δf_2	-0.1073	-0.0728	-0.0229	-0.0018	-0.0011	
		ΔP_{tie}	-0.0411	-0.0293	0.0091	-0.0021	0.0013	
OS		Δf_1	0.0000	0.0000	0.0127	0.0089	0.0031	
		Δf_2	0.0000	0.0000	2.52E-07	1.75E-06	4.85E-14	
		ΔP_{tie}	0.0000	0.0000	2.90E-07	2.14E-06	9.25E-15	
Ess		Δf_1	-5.77E-06	-2.11E-07	3.02E-15	-3.05E-15	-9.70E-15	
		Δf_2	-8.17E-06	-4.00E-07	4.92E-15	7.68E-15	-1.09E-14	
		ΔP_{tie}	-2.14E-06	-1.57E-07	2.09E-15	3.34E-15	6.27E-15	
ITSE			0.2750	0.0964	0.0035	0.0002	6.53E-05	
Case3		$T_s(s)$ (± 0.0005)	Δf_1	14.4865	8.8066	2.3670	1.9632	1.7067
			Δf_2	14.0837	9.3278	3.5693	1.4908	1.2015
	ΔP_{tie}		10.8201	7.2401	2.9088	1.4343	1.3433	
	US	Δf_1	-0.1987	-0.1783	-0.0868	-0.0355	-0.0251	
		Δf_2	-0.1760	-0.1045	-0.0332	-0.0179	-0.0123	
		ΔP_{tie}	-0.0184	-0.0177	-0.0073	-0.0011	-0.0007	
	OS	Δf_1	0.0000	0.0000	0.0078	0.0080	0.0025	
		Δf_2	0.0000	0.0000	2.21E-07	0.0027	0.0005	
		ΔP_{tie}	0.0017	0.0000	1.77E-07	1.10E-06	5.03E-15	
	Ess	Δf_1	-2.67E-05	-3.61E-07	2.85E-15	-3.11E-14	-9.17E-14	
		Δf_2	-2.76E-05	-4.84E-07	2.84E-15	-3.10E-15	-9.07E-15	
		ΔP_{tie}	1.14E-05	-1.03E-07	2.09E-15	3.36E-15	-9.36E-17	
	ITSE		0.6332	0.1514	0.0044	0.0003	0.0001	



(a)



(b)

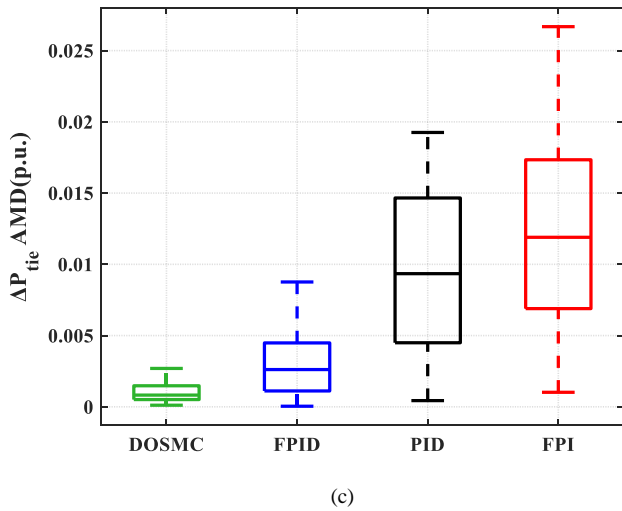


Fig. 17. Robustness assessment under different strategies. (a) AMD in frequency of area-1. (b) AMD in frequency of area-2. (c) AMD in tie-line power deviation.

reasonable and ideal range. Therefore, it can be concluded that the system controlled by the proposed method has better resistance to load changes.

(ii) T_G 、 T_T change and T_{12} change

To further test the robustness of the proposed controller, sensitivity analysis is performed by introducing uncertainties into the system model parameters. The system was analyzed with a 10% step load change applied in area-1 under rated operating conditions. System parameters are increased from -20% to 40% of their value in steps of 10%. The performance indicators of the system are shown in TABLE V. Through the critical examination of TABLE V, it can be obtained that the performance indicators (more or less) are basically the same under the conditions of nominal conditions and system parameter changes. The fluctuation results of the frequency deviation caused by the change of the time constant of the steam turbine governor and the synchronization coefficient of the tie-line are shown in Fig. 19. It can be seen from the figure that the system frequency deviations are all within a reasonable range, the changes of Δf_i and ΔP_{12} are less affected by the change of T_G , T_T and synchronous torque T_{12} , and the change of T_G has little effect on the system response, which can be almost ignored.

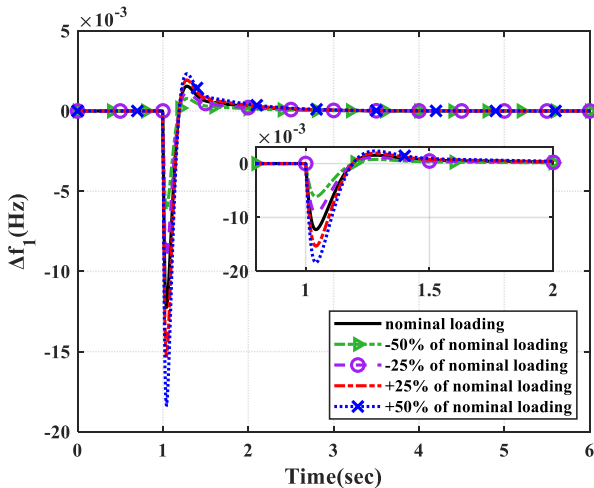
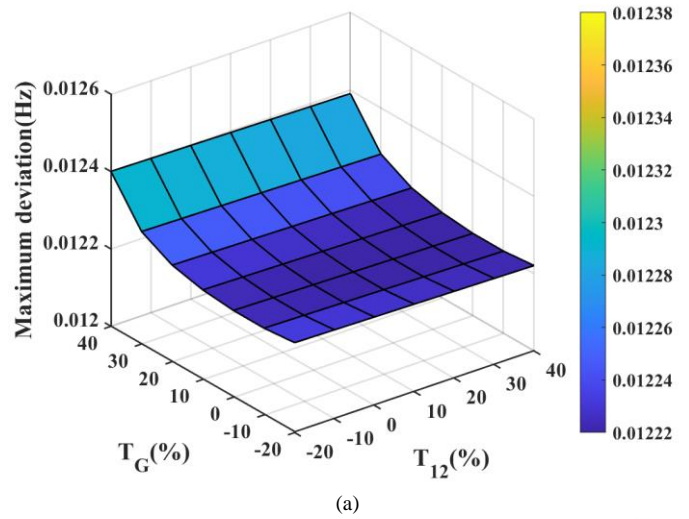
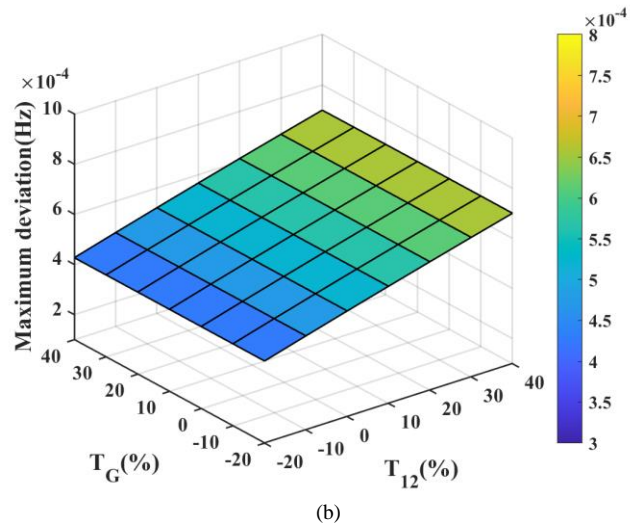


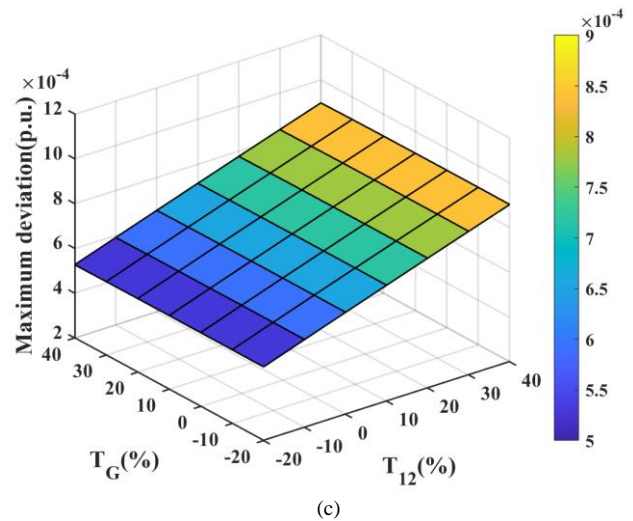
Fig. 18. Frequency deviation of area-1 for different load changes in area-1



(a)



(b)



(c)

Fig. 19. Impact of T_G and T_{12} on the AMD. (a) Frequency deviation of area-1. (b) Frequency deviation of area-2. (c) Tie-line power deviation.

However, AMD fluctuates with the changes of T_{12} and T_T , showing a monotonic trend.

On the whole, large changes in system parameters and loading conditions show little effect on the system response, and the proposed control strategy provides satisfactory robustness and stability. Furthermore, the optimal values of the controller parameters at the nominal load obtained at the nominal parameters do not need to be reset when the system load or system parameters vary greatly.

TABLE V
PERFORMANCE INDICATORS UNDER DIFFERENT SYSTEM PARAMETER CONDITIONS

Conditional Variation variable (%)	ITSE	$T_s (\pm 0.0005)$			US			OS			Ess			
		Δf_1	Δf_2	ΔP_{tie}	Δf_1	Δf_2	ΔP_{tie}	Δf_1	Δf_2	ΔP_{tie}	Δf_1	Δf_2	ΔP_{tie}	
Nominal	0	1.61E-05	1.64	1.46	1.36	-0.0123	-0.0005	-0.0007	0.0015	0.0000	0.0000	8.78E-08	-9.11E-08	-4.46E-08
Load	50	3.63E-05	1.91	1.86	1.60	-0.0184	-0.0008	-0.0010	0.0023	0.0000	0.0000	1.32E-07	-1.37E-07	-6.70E-08
	25	2.52E-05	1.79	1.72	1.49	-0.0153	-0.0007	-0.0008	0.0019	0.0000	0.0000	1.10E-07	-1.14E-07	-5.58E-08
	-25	9.07E-06	1.48	1.47	1.36	-0.0092	-0.0004	-0.0005	0.0012	0.0000	0.0000	6.58E-08	-6.83E-08	-3.35E-08
	-50	4.03E-06	1.39	1.46	1.36	-0.0061	-0.0003	-0.0003	0.0008	0.0000	0.0000	4.39E-08	-4.56E-08	-2.23E-08
	40	1.61E-05	1.64	1.47	1.36	-0.0123	-0.0005	-0.0007	0.0015	0.0000	0.0000	7.54E-07	-7.82E-07	-3.90E-07
T_G	20	1.61E-05	1.64	1.47	1.36	-0.0123	-0.0005	-0.0007	0.0016	0.0000	0.0000	7.54E-07	-7.82E-07	-3.90E-07
	-20	1.61E-05	1.64	1.47	1.36	-0.0122	-0.0005	-0.0007	0.0016	0.0000	0.0000	7.54E-07	-7.82E-07	-3.90E-07
	40	1.08E-05	1.18	1.50	1.37	-0.0127	-0.0004	-0.0005	0.0006	0.0000	0.0000	1.21E-06	-1.28E-06	-6.38E-07
T_T	20	1.71E-05	1.67	1.50	1.37	-0.0123	-0.0005	-0.0007	0.0017	0.0000	0.0000	7.01E-07	-7.25E-07	-3.61E-07
	-20	2.14E-05	1.74	1.56	1.39	-0.0124	-0.0006	-0.0008	0.0026	0.0000	0.0000	4.86E-07	-4.97E-07	-2.45E-07
	40	1.72E-05	1.70	1.64	1.45	-0.0123	-0.0007	-0.0009	0.0017	2.44E-06	3.29E-06	-1.30E-07	1.41E-07	3.44E-08
T_{12}	20	1.60E-05	1.62	1.39	1.34	-0.0123	-0.0005	-0.0006	0.0015	0.0000	0.0000	1.25E-06	-1.29E-06	-7.00E-07
	-20	1.55E-05	1.54	3.31	1.25	-0.0123	-0.0004	-0.0005	0.0014	0.0000	0.0000	5.09E-06	-5.17E-06	-3.34E-06

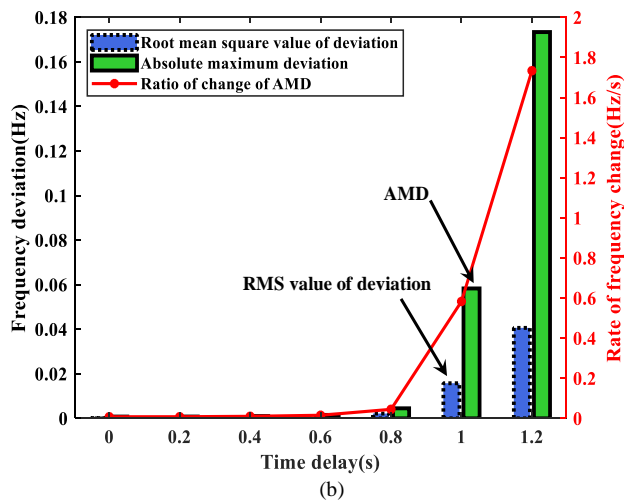
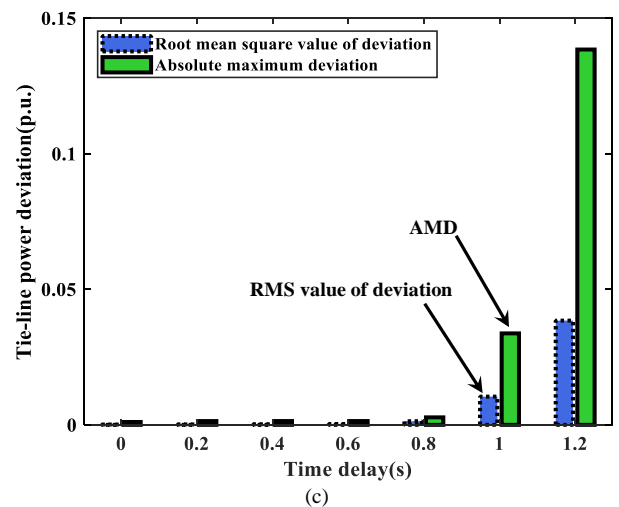
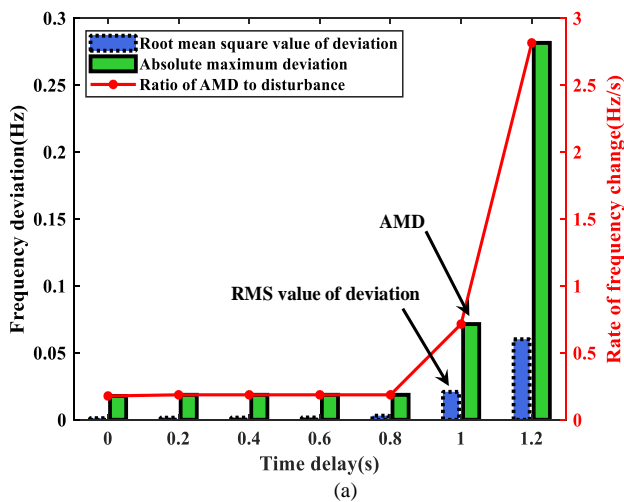


Fig. 20. Performance analysis of controller for different time delays. (a) Frequency deviation of area-1. (b) Frequency deviation of area-2. (c) Tie-line power deviation.

Case D: Impact of Communication Delay

Delays in communication links are a common feature in wide-area control of power systems. Excessive delays may affect the performance of the controller. To examine the effect of delay on the performance of this controller, a delay link varying from 0s to 1.2s is introduced in the control loop. Fig. 20 shows the performance indicators of the proposed controller, such as the frequency deviation and tie-line power deviation, with a 10% load change applied in area-1 when the communication delay changes. As can be seen from the figure, as long as the communication delay is below 0.8s, the frequency deviation fluctuation is small, and

the adjustment performance of the controller remains within an acceptable range. When the communication delay increases from 0.8s to 1.2s, the performance index rises dramatically and grows exponentially. For example, the AMD value of Δf_1 changes from 0.0187 (Hz) in $t=0.8s$ to 0.2815 (Hz) in $t=1.2s$, and the frequency change rates of Δf_1 and Δf_2 are also delayed with time sharply increase. It can be seen from the figure when the system frequency deviation is within $\pm 20\%$, the allowable time delay limit $\eta = 1.13s$ to ensure the stability of the power system under the proposed control method.

C. Three-area power system with GRC connected wind turbine generators

To test the performance of the proposed control strategy

in a multi-area power interconnection system with nonlinear and wind energy links, simulations are performed using the non-equivalent three-region power system with GRC nonlinear links and wind turbines shown in Fig. 21. The system consists of three interconnected non-reheating power stations, with the control power set at 2000Mw/ 5000Mw/ 8000Mw for the 1/ 2/ 3 area. The nominal values of the system parameters are shown in Appendix B. There are three kinds of case studies. Case A is the system performance analysis under step disturbance. Case B is the system performance analysis under random load. Case C is the influence of random wind speed on the system stability.

In the actual power system relying on the steam generator for power supply, when the load produces a large disturbance, in order to avoid the impacts of temperature,

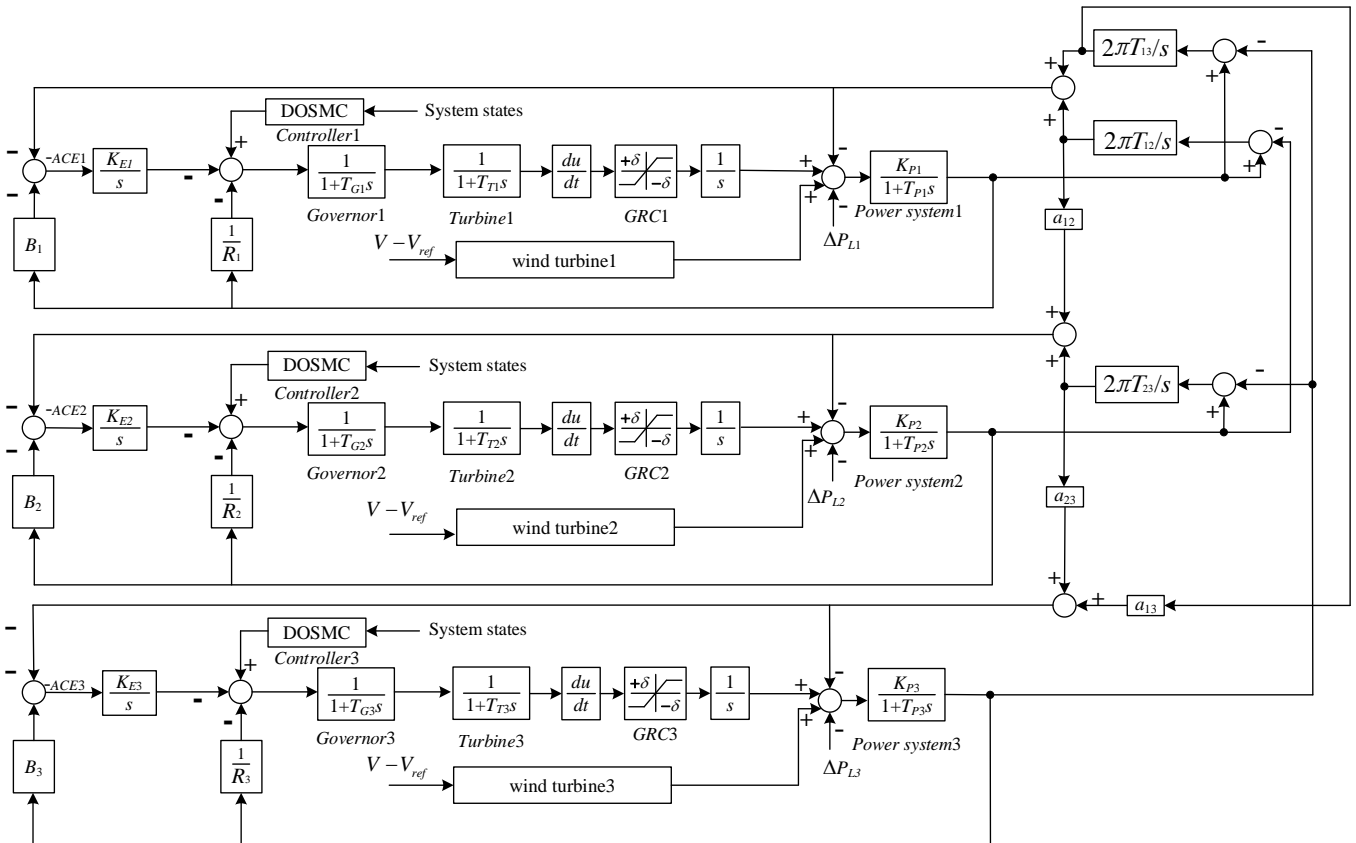


Fig. 21. Transfer function model of three-area power system with GRC connected WTGs

TABLE VI
PERFORMANCE INDICATORS OF THREE-AREA POWER SYSTEM WITH GRC UNDER DIFFERENT CONTROL METHODS

	MFO PI[39]						GWO PID[40]					
	Δf_1	Δf_2	Δf_3	ΔP_{12}	ΔP_{13}	ΔP_{23}	Δf_1	Δf_2	Δf_3	ΔP_{12}	ΔP_{13}	ΔP_{23}
$T_s(\pm 0.0001)$	14.61	12.01	10.59	10.84	10.92	7.14	8.01	9.69	8.79	6.92	6.55	7.02
US	-0.0204	-0.0067	-0.0061	-0.0067	-0.0070	-0.0005	-0.0160	-0.0042	-0.0042	-0.0045	-0.0048	-0.0004
OS	0.0133	0.0019	0.0019	0.0011	0.0010	0.0002	0.0101	0.0016	0.0019	0.0006	0.0008	0.0003
E_{ss}	1.02E-05	7.62E-07	-2.91E-06	2.62E-06	1.55E-06	-1.07E-06	-7.41E-07	-7.54E-07	3.97E-07	-9.57E-08	7.08E-08	1.67E-07
	IHBA DOSMC						IHBA DOSMC Without GRC					
	Δf_1	Δf_2	Δf_3	ΔP_{12}	ΔP_{13}	ΔP_{23}	Δf_1	Δf_2	Δf_3	ΔP_{12}	ΔP_{13}	ΔP_{23}
$T_s(\pm 0.0001)$	3.37	2.71	3.10	2.74	2.85	7.14	1.89	0.00	0.00	1.23	1.24	0.00
US	-0.0087	-0.0008	-0.0006	-0.0017	-0.0018	-8.71E-05	-0.0015	-3.30E-05	-2.18E-05	-0.0001	-0.0001	-3.33E-06
OS	0.0029	5.61E-05	8.64E-06	7.23E-05	5.67E-05	3.66E-06	0.0003	6.85E-07	1.08E-15	4.20E-16	4.06E-16	1.72E-16
E_{ss}	1.71E-13	-6.49E-15	-3.73E-15	-8.58E-15	-8.75E-15	-1.65E-16	2.89E-15	7.66E-16	3.30E-16	3.33E-16	3.46E-16	1.38E-17

pressure and other factors on the power generation system, combined with the physical structure limitations of the generator itself, it is necessary to restrain the power generation rate of the generator to ensure the safe and stable operation of the system. This limitation is called Generation Rate Constraint (GRC), and in general, the typical constraint is 3%/min for thermal power [41].

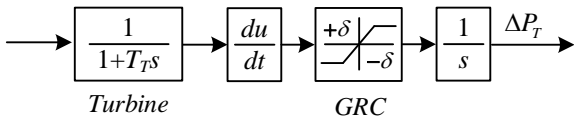


Fig. 22. Open loop model of GRC

Case A. Comparisons

In order to verify the performance of the proposed control strategy in a multi-area power interconnection system with nonlinearity, the MFO optimized PI [39] and the GWO optimized PID [40] control methods are used for comparative analysis to prove the superiority of the proposed control method. The proposed control method is used for comparison without GRC to analyze the influence of GRC on the system.

When $t=1$ s, the SLP of area-1 is 1%, the wind speed is the rated wind speed of 12(m/s), the response curve of the system frequency deviation ($\Delta f_1, \Delta f_2, \Delta f_3$) and the incremental change of tie-line power deviation response curves are shown in Fig. 23. The relevant performance indicators of the system are shown in TABLE VI, including dynamic indicators settlement time (T_s), steady-state error (E_{ss}), peak undershoot (US) and peak overshoot (OS).

From the analysis of the figure and table, it can be obtained: i) The proposed control strategy DOSMC has a satisfactory effect in the secondary regulation of LFC when the load demand imbalance suddenly occurs in the three-region power system with the non-equal capacity and GRC nonlinear links. At the same time, it has a faster response speed and a stronger damping effect compared to other methods, which can quickly restore the system frequency to the nominal state with a lower fluctuation amplitude. The results show that the proposed control strategy has a better ability to suppress the nonlinearity of GRC. ii) Comparing the data and graphs of the two cases with and without GRC nonlinear links, it can be concluded that nonlinear factors have a significant impact on the dynamic performance of the power system. Under the same conditions, the performance

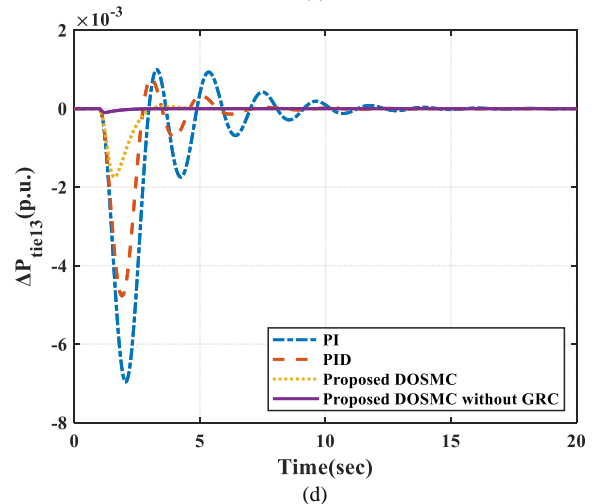
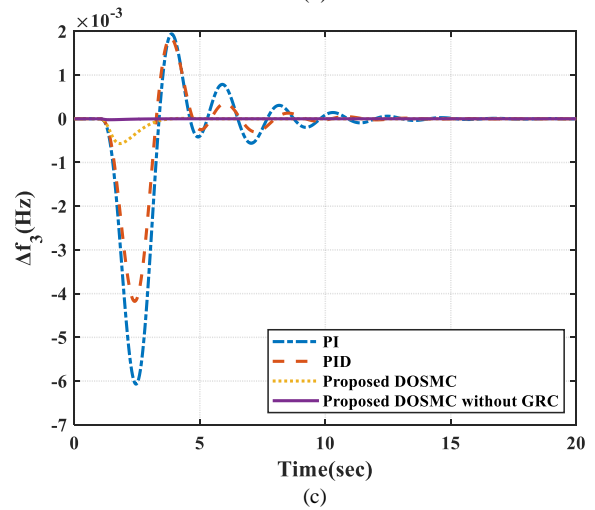
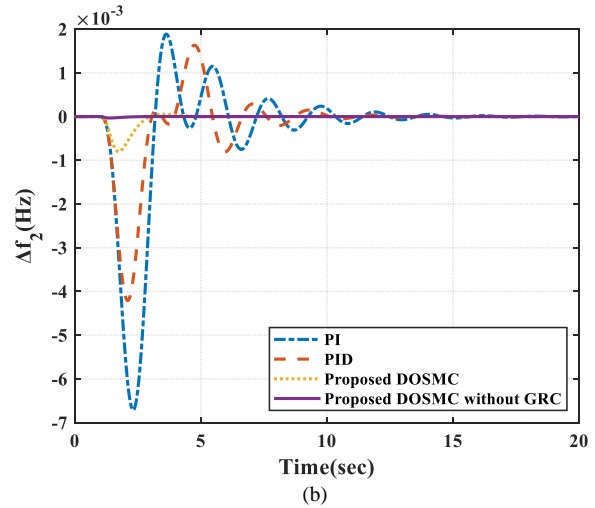
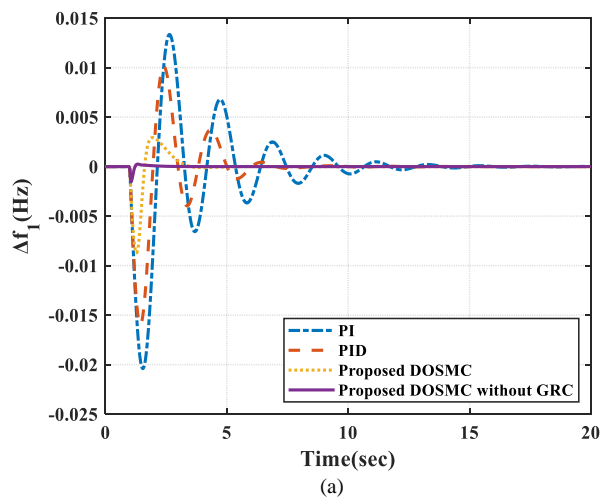


Fig. 23. Deviations of different strategies for 1% step load change. (a) Frequency deviation of area-1. (b) Frequency deviation of area-2. (c) Frequency deviation of area-3. (d) Tie-line power deviation of area-1 and area-3.

indicators of the nonlinear system with GRC are all worse than those of the linear system. The most obvious is that the US, OS and T_s of the former are 5 to 10 times larger than those of the latter.

Case B. Random load

Actual loads are usually random loads. In order to further evaluate the stability of the proposed strategy, a random step load change of 100s shown in Fig. 25 is placed in the area-1 of the system. As can be seen from the frequency offset response curve in Fig. 24, the proposed controller can adjust

the system faster than PID and PI controllers. Prevent frequency offset and tie-line power deviation from large fluctuations and make them rapidly reduce to near zero showing a good transient response. The results show that the proposed strategy can compensate the imbalance of the system and make the power system better able to withstand perturbations under more stringent load conditions.

To be closer to the actual load of the power system, load conditions that mix large deterministic load demand with small stochastic power fluctuations are considered. The random load shown in Fig. 26 is applied to area-1 for the simulation.

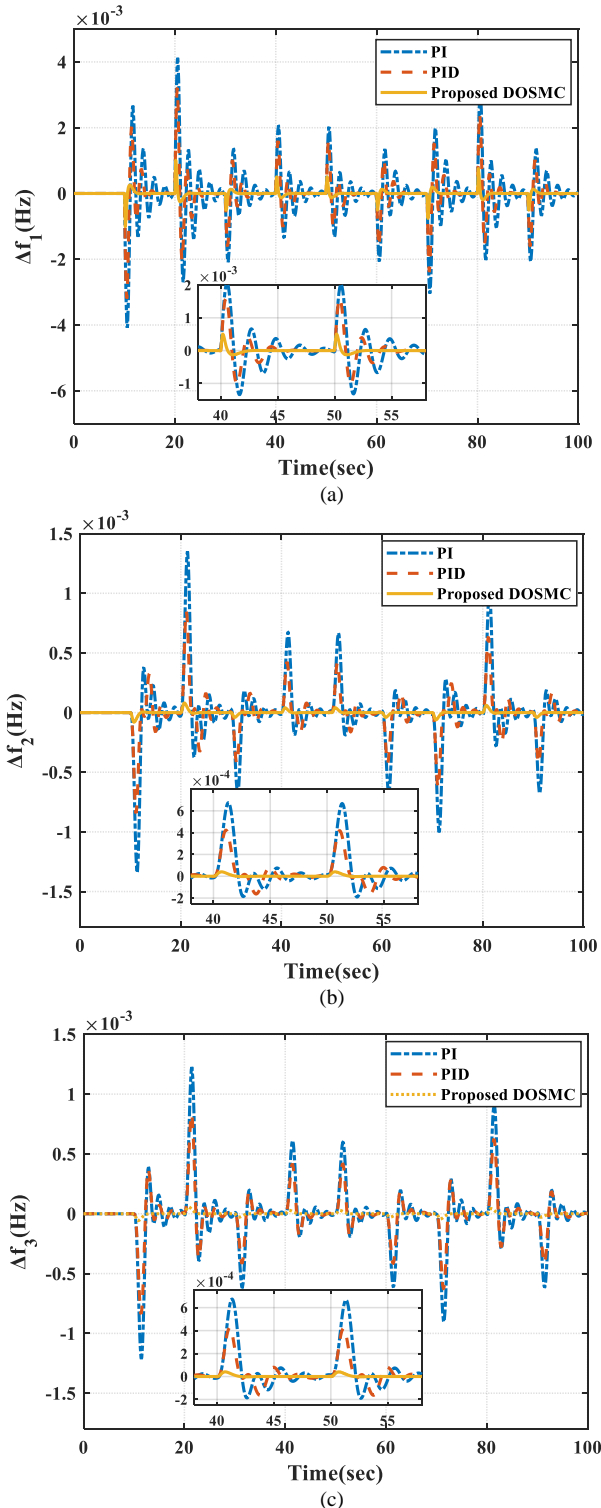


Fig. 24. Deviations of different strategies for random step load change. (a) Frequency deviation of area-1. (b) Frequency deviation of area-2. (c) Frequency deviation of area-3.

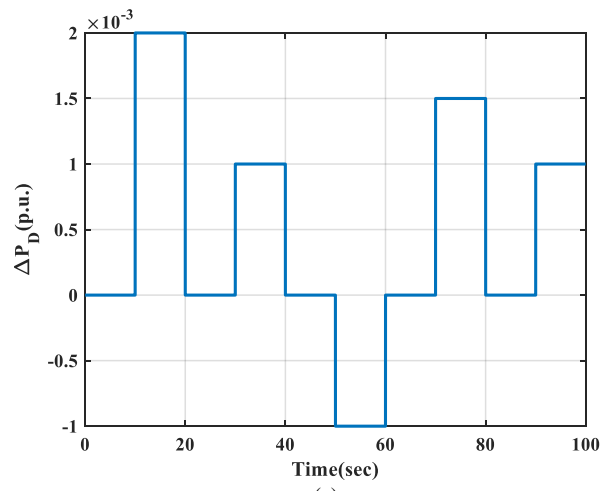


Fig. 25. Random step load variation in area-1

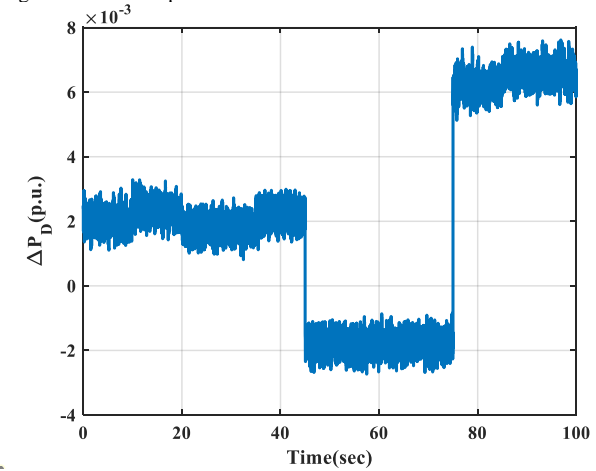


Fig. 26. Mixed random load variation in area-1

As can be seen from the frequency response curve in Fig. 27, the maximum frequency deviation of the system is 30% of the applied disturbance. And the high-frequency response range of the system is $[-0.00015, 0.0002]$, which is only 10% of the random power fluctuation. It is shown that the three-area power system with nonlinear links still has an excellent ability to withstand high-frequency stochastic perturbations under the control of this strategy.

Case C. Wind change

The intermittent nature of natural wind energy determines the unpredictable fluctuation of wind power. In order to explore the influence of wind speed on the system frequency after wind power is connected to the grid, the rated wind speed of wind turbines in area-1 is set to 12(m/s). Based on this, random noise is introduced to simulate a random variable wind speed, as shown in Fig. 28. The results of the frequency dynamic response for each area of the system at random wind speed are shown in Fig. 29. The change of wind speed causes the fan output power ΔP_W to fluctuate back and forth in $[-0.02, 0.01]$, while the system frequency fluctuation range is all in $[-0.001, 0.0015]$, which is only 15% of the power fluctuation. It turns out that the frequency fluctuation trends of the three regions are almost the same. Experimental results show that the use of controllable conventional energy sources such as a thermal power as a frequency modulation plant can effectively reduce the frequency fluctuations and effects caused by wind power grid connections, thus improving the stability of the system.

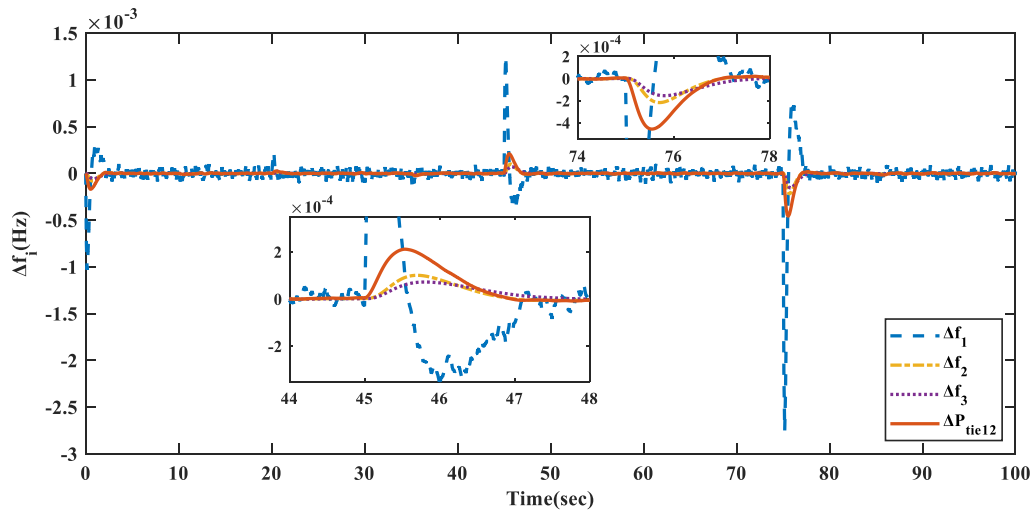


Fig. 27. Frequency deviations and tie-line power deviation for mixed random load change in area-1

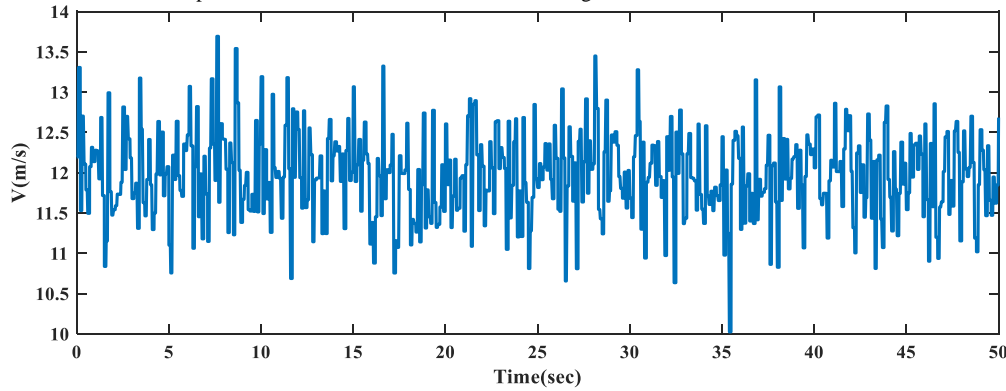


Fig. 28. Random wind speed in area-1

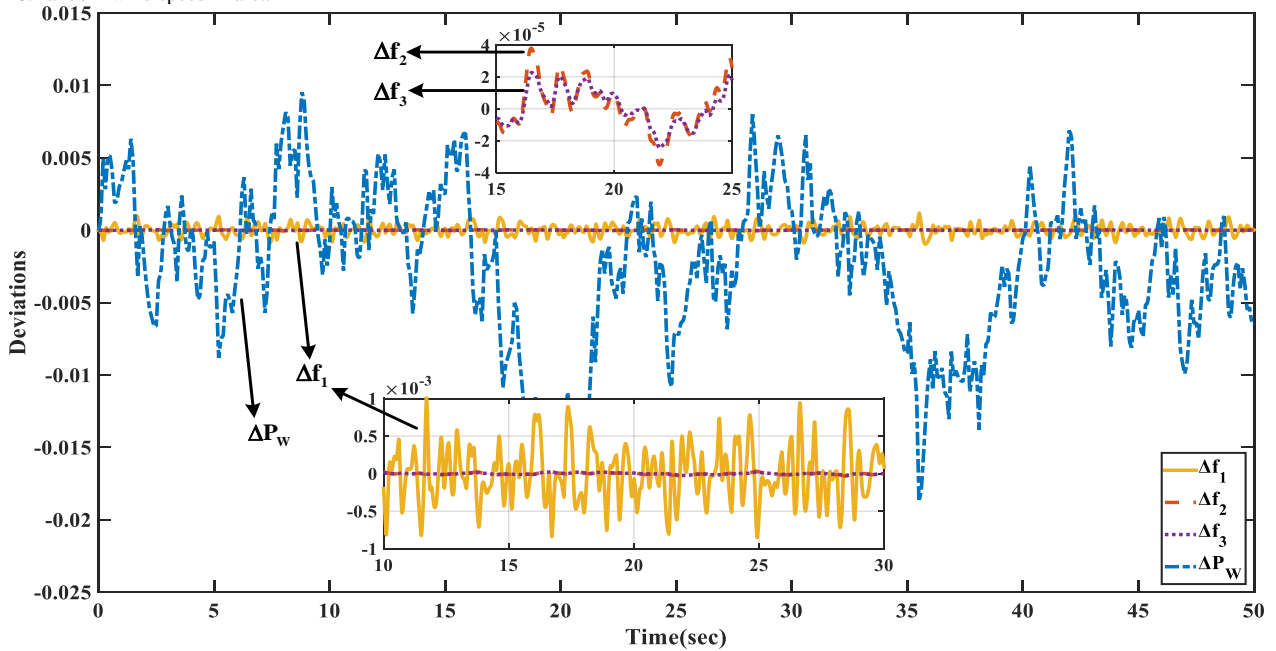


Fig. 29. Frequency deviations of three-area power system and the fan out power fluctuation under random wind speed

V. CONCLUSION

This paper presents an observer-based integral-type sliding mode control strategy optimized by improved honey badger algorithm for the frequency regulation problem of a multi-region nonlinear power system accessed to WTGs under load disturbance and parameter uncertainties. Parametric uncertainties are modeled into the power system model, and then a proportional-integral sliding mode control method is proposed to control the load frequency of the power systems under study. The sliding mode controller is

reconstructed based on the lumped perturbations estimated by the disturbance observer. Meanwhile, the corresponding sliding mode control design, the control method based on the improved HBA is further developed. Simulation results have shown that the multi-area power systems perform better under the proposed control strategy. The superior robustness properties of the proposed control method over alternative control methods are demonstrated to handle nonlinearities and various sources of uncertainty, including

uncertainties in the values of load variations, model parameters and the output power of wind turbine generators. In addition, the system performance tests under different time delays show that the proposed control scheme maintains the superior performance over a wide range of delays in the communication links.

APPENDIX

Appendix A: nominal parameters of two-area non-reheat power system [10, 16, 37, 38]

$P_{r1} = P_{r2} = 2000$ MW, $P_{L1} = P_{L2} = 1000$ MW, $f = 60$ Hz; $T_{T1} = T_{T2} = 0.3$ s, $T_{G1} = T_{G2} = 0.08$ s, $B_1 = B_2 = 0.425$ p.u.MW/Hz, $T_{P1} = T_{P2} = 20$ s, $K_{P1} = K_{P2} = 120$ Hz/p.u.MW, $R_1 = R_2 = 2.4$ Hz/p.u., $T_{12} = 0.545$ p.u., $K_{E1} - K_{E2} = 10$.

Appendix B: nominal parameters of unequal three-area power system with GRC connected WTG [22, 41, 42]

Power system: $P_{r1} = 2000$ MW; $P_{r2} = 5000$ MW; $P_{r3} = 8000$ MW; $B_1 = B_2 = B_3 = 0.425$ p.u.MW/Hz; $R_1 = R_2 = R_3 = 2.0$ Hz/p.u.; $T_{G1} = T_{G2} = T_{G3} = 0.08$ s; $T_{T1} = T_{T2} = T_{T3} = 0.3$ s; $T_{P1} = T_{P2} = T_{P3} = 20$ s; $K_{P1} = K_{P2} = K_{P3} = 120$ Hz/p.u.; $T_{12} = T_{13} = T_{23} = 0.545$ p.u.; $a_{12} = -2/5$; $a_{13} = -2/8$; $a_{23} = -5/8$.

WTG system: $\rho = 1.25$ kg/m³, $A_r = 1735$ m², $R = 23.5$ m; $\omega_r = 3.14$ rad/s, $K_{WT} = 1$, $T_{WT} = 1.5$ s.

REFERENCES

- X. Yuan, C. Chen, M. Jiang, Y. Yuan, "Prediction interval of wind power using parameter optimized Beta distribution based LSTM model," *Applied Soft Computing*, vol. 82, p. 105550, 2019.
- G. Chen, J. Qian, Z. Zhang, S. Li, "Application of modified pigeon-inspired optimization algorithm and constraint-objective sorting rule on multi-objective optimal power flow problem," *Applied Soft Computing*, vol. 92, p. 106321, 2020.
- T. Wen, "Unified Tuning of PID Load Frequency Controller for Power Systems via IMC," *Energy Conversion & Management*, vol. 50, no. 6, pp. 1465-1472, 2009.
- H. A. Yousef, K. AL-Kharusi, M. H. Albadi, N. Hosseinzadeh, "Load Frequency Control of a Multi-Area Power System: An Adaptive Fuzzy Logic Approach," *IEEE Transactions on Power Systems*, vol. 29, no.4, pp. 1822-1830, 2014.
- Z. Yan, Y. Xu, "Data-Driven Load Frequency Control for Stochastic Power Systems: A Deep Reinforcement Learning Method with Continuous Action Search," *IEEE Transactions on Power Systems*, vol. 34, no. 2, pp. 1653-1656, 2019.
- A. M. Ersdal, L. Imsland, K. Uhlen, "Model Predictive Load-Frequency Control," *IEEE Transactions on Power Systems*, vol. 31, no. 1, pp. 777-785, 2015.
- G. Chen, F. Qin, H. Long, X. Zeng, P. Kang, J. Zhang, "Fuzzy PID Controller Optimized by Improved Gravitational Search Algorithm for Load Frequency Control in Multi-area Power System," *IAENG International Journal of Computer Science*, vol. 49, no. 1, pp. 125-139, 2022.
- G. Tang, Z. Xu, H. Dong, Q. Xu, "Sliding Mode Robust Control Based Active-Power Modulation of Multi-Terminal HVDC Transmissions," *IEEE Transactions on Power Systems*, vol. 31, no. 2, pp. 1614-1623, 2016.
- K. Vrdoljak, N. Peri, I. Petrovi, "Sliding mode based load-frequency control in power systems," *Electric Power Systems Research*, vol. 80, no. 5, pp. 514-527, 2010.
- Y. Mi, Y. Fu, C. Wang, P. Wang, "Decentralized Sliding Mode Load Frequency Control for Multi-Area Power Systems," *IEEE Transactions on Power Systems*, vol. 28, no. 4, pp. 4301-4309, 2013.
- D. Qian, S. Tong, H. Liu, X. Liu, "Load frequency control by neural-network-based integral sliding mode for nonlinear power systems with wind turbines," *Neurocomputing*, vol. 173, pp. 875-885, 2016.
- Z. Deng and C. Xu, "Frequency Regulation of Power Systems with a Wind Farm by Sliding-Mode-Based Design," *IEEE/CAA Journal of Automatica Sinica*, vol. 9, 2022, in press.
- L. Liu, Z. Zhang, G. Chen, H. Zhang, "Resource Management of Heterogeneous Cellular Networks with Hybrid Energy Supplies: A Multi-Objective Optimization Approach," *IEEE Transactions on Wireless Communications*, vol. 20, no. 7, pp. 4392-4405, 2021.
- J. Qian, P. Wang, C. Pu and G. Chen, "Joint application of multi-object beetle antennae search algorithm and BAS-BP fuel cost forecast network on optimal active power dispatch problems," *Knowledge-Based Systems*, vol. 226, p. 107149, 2021.
- G. Chen, X. Tan, Z. Zhang, Z. Sun, "Parameter optimization of pid sliding mode controller for hydraulic turbine regulating system based on IFABC algorithm," *Engineering Letters*, vol. 28, no. 1, pp. 168-179, 2020.
- E. S. Ali, S. M. Abd-Elazim, "BFOA based design of PID controller for two area Load Frequency Control with nonlinearities," *International Journal of Electrical Power & Energy Systems*, vol. 51, no. 51, pp. 224-231, 2013.
- M. Shouran, F. Anayi and M. Packianather, "The Bees Algorithm Tuned Sliding Mode Control for Load Frequency Control in Two-Area Power System," *Energies*, vol. 14, no.18, pp. 1-28, 2021.
- B. Mohanty, "TLBO optimized sliding mode controller for multi-area multi-source nonlinear interconnected AGC system," *International Journal of Electrical Power & Energy Systems*, vol. 73, pp. 872-881, 2015.
- K. Premkumar, B. V. Manikandan, "Bat algorithm optimized fuzzy PD based speed controller for brushless direct current motor," *Engineering Science and Technology, an International Journal*, vol. 19, no. 2, pp. 818-840, 2016.
- C. Mu, Y. Tang and H. He, "Improved Sliding Mode Design for Load Frequency Control of Power System Integrated an Adaptive Learning Strategy," *IEEE Transactions on Industrial Electronics*, vol. 64, no. 8, pp. 6742-6751, 2017.
- P. Wang, R. Billinton, "Reliability benefit analysis of adding WTG to a distribution system," *IEEE Transactions on Energy Conversion*, vol. 16, no. 2, pp. 134-139, 2001.
- A. Y. Abdelaziz, A. M. Kassem, "Reactive power control for voltage stability of standalone hybrid wind - diesel power system based on functional model predictive control," *Renewable Power Generation IET*, vol. 8, no. 8, pp. 887-899, 2014.
- D. J. Lee, L. Wang, "Small-Signal Stability Analysis of an Autonomous Hybrid Renewable Energy Power Generation/Energy Storage System Part I: Time-Domain Simulations," *IEEE Transactions on Energy Conversion*, vol. 23, no. 1, pp. 311-320, 2008.
- C. Mu, C. Sun, W. Xu, "Fast sliding mode control on air-breathing hypersonic vehicles with transient response analysis," *Proceedings of the Institution of Mechanical Engineers Part I Journal of Systems & Control Engineering*, vol. 230, no. 11, pp. 23-34, 2015.
- C. Mu, W. Xu, C. Sun, "On switching manifold design for terminal sliding mode control," *Journal of the Franklin Institute*, vol. 353, no. 7, pp. 1553-1572, 2016.
- W. H. Chen, "Disturbance observer based control for nonlinear systems," *IEEE/ASME Transactions on Mechatronics*, vol. 9, no. 4, pp. 706-710, 2004.
- J. Yang, S. Li, X. Yu, "Sliding-Mode Control for Systems With Mismatched Uncertainties via a Disturbance Observer," *IEEE Transactions on Industrial Electronics*, vol. 60, no. 1, pp. 160-169, 2013.
- F. A. Hashim, E. H. Houssein, K. Hussain, S. M. Mai, W. Al-Atabany, "Honey Badger Algorithm: New Metaheuristic Algorithm for Solving Optimization Problems," *Mathematics and Computers in Simulation*, vol. 192, pp. 84-110, 2022.
- E. Han, N. Ghadimi, "Model identification of proton-exchange membrane fuel cells based on a hybrid convolutional neural network and extreme learning machine optimized by improved honey badger algorithm," *Sustainable Energy Technologies and Assessments*, vol. 52, p. 102005, 2022.
- L. Li, Q. Shen, M. Tseng, S. Luo, "Power system hybrid dynamic economic emission dispatch with wind energy based on improved saifish algorithm," *Journal of Cleaner Production*, vol. 316, p. 128318, 2021.
- A. Nickabadi, M. M. Ebadzadeh, R. Safabakhsh, "A novel particle swarm optimization algorithm with adaptive inertia weight," *Applied Soft Computing*, vol. 11, no. 4, pp. 3658-3670, 2011.
- H. Haklı, H. Uğuz, "A novel particle swarm optimization algorithm with Levy flight," *Applied Soft Computing*, vol. 23, pp. 333-345, 2014.
- G. Chen, Z. Li, Z. Zhang, and Li S, "An Improved ACO Algorithm Optimized Fuzzy PID Controller for Load Frequency Control in Multi Area Interconnected Power Systems," *IEEE Access*, vol. 8, pp. 6429-6447, 2020.
- Y. Tang, P. Ju, H. He, C. Qin, F. Wu, "Optimized Control of DFIG-Based Wind Generation Using Sensitivity Analysis and Particle Swarm Optimization," *IEEE Transactions on Smart Grid*, vol. 4, no. 1, pp. 509-520, 2013.
- Y. D. Valle, G. K. Venayagamoorthy, S. Mohagheghi, J. C. Hernandez, R. G. Harley, "Particle Swarm Optimization: Basic Concepts, Variants and Applications in Power Systems," *IEEE*

Transactions on Evolutionary Computation, vol. 12, no. 2, pp. 171-195, 2008.

- [36] Y. Arya, "Automatic generation control of two-area electric power systems via optimal fuzzy PID with filter plus double integral controller," *Journal of the Franklin Institute*, vol. 355, no. 11, pp. 4583-4617, 2018.
- [37] R. K. Sahu, S. Panda, G. Sekhar, "A novel hybrid PSO-PS optimized fuzzy PI controller for AGC in multi area interconnected power systems," *International Journal of Electrical Power & Energy Systems*, vol. 64, no. 1, pp. 880-893, 2015.
- [38] M. Gheisarnejad, "An effective hybrid harmony search and cuckoo optimization algorithm based fuzzy PID controller for load frequency control," *Applied Soft Computing*, vol. 65, pp. 121-138, 2018.
- [39] D. K. Lal, K. K. Bhoi, A. K. Barisal, "Performance evaluation of MFO algorithm for AGC of a multi area power system," in *International Conference on Signal Processing, Communication, Power and Embedded System 2016*, pp. 903-908.
- [40] R. K. Mallick, F. Haque, R. R. Rout, M. K. Debnath, "Application of grey wolves-based optimization technique in multi-area automatic generation control," in *2016 International Conference on Electrical, Electronics, and Optimization Techniques (ICEEOT) 2016*, pp. 269-274.
- [41] D. Guha, P. K. Roy, S. Banerjee, "Application of backtracking search algorithm in load frequency control of multi-area interconnected power system," *Ain Shams Engineering Journal*, vol. 9, no. 2, pp. 257-276, 2016.
- [42] J. Nanda, S. Mishra, L. C Saikia, "Maiden Application of Bacterial Foraging-Based Optimization Technique in Multiarea Automatic Generation Control," *IEEE Transactions on Power Systems*, vol. 24, no. 2, pp. 602-609, 2009.
- [43] N. K. Jena, S. Sahoo, B. K. Sahu, J. Ranjan Nayak, K. B. Mohanty, "Fuzzy adaptive selfish herd optimization based optimal sliding mode controller for frequency stability enhancement of a microgrid," *Engineering Science and Technology, an International Journal*, vol. 33, p. 101071, 2022.